GROWTH RATE SIMULATIONS OF INSTABILITY MECHANISMS AT LOW AND MID–LATITUDES FOR EXPLAINING EQUATORIAL SPREAD *F*

BY

TIMOTHY MATTHEW DULY

THESIS

Submitted in partial fulfillment of the requirements
for the degree of Master of Science in Electrical and Computer Engineering
in the Graduate College of the
University of Illinois at Urbana-Champaign, 2011

Urbana, Illinois

Adviser:

Associate Professor Jonathan J. Makela

ABSTRACT

One of the ongoing fields of ionospheric research is studying the characteristics and behavior of Equatorial Spread F (ESF). The general seasonalities of ESF occurrence are well known, but much work remains to be done in learning its day–to–day variability. Understanding the complexities of the ionosphere is important for communication systems whose signals pass through Earth's atmosphere because knowledge of outages or detriments to the system benefit the user.

This thesis presents climatological modeling of ionospheric instabilities for both low– and mid–latitude locations. The purpose of the modeling is to provide simulation support for observations of mid–latitude medium–scale traveling ionospheric disturbances (MSTIDs) coupling into equatorial regions and initiating ESF there. It is proposed that the polarization electric fields of MSTIDs provide the seed mechanism to initiate ESF for post–midnight, solar minimum times.

To begin, background information on the ionosphere is presented and instability mechanisms are investigated. Then, models of the growth rate of the instabilities for both low and mid–latitudes are developed from theory. The growth rate models are then compared with radar data from Christmas Island. The simulations will help validate the observational evidence of MSTIDs seeding ESF.

To my parents, whose love and encouragement have been perpetual in my life

ACKNOWLEDGMENTS

I would like to thank my adviser, Professor Jonathan Makela, for his continuing support, patience, and advice as I conduct research at the graduate level. It has truly made the experience an enjoyable one. I would also like to thank the National Science Foundation, who supported my studies through CAREER grant ATM 06-44654. Finally, thank you to my fellow graduate students in the Remote Sensing and Space Sciences group at Illinois who have helped with all aspects of graduate school life: Daniel Fisher, Thomas Gehrels, Peter Hedlund, Yiyi Huang, Uday Kanwar, James Law, Tony Mangognia, Serge Minin, and Pablo Reyes.

TABLE OF CONTENTS

LIST OF TABLES

LIST OF FIGURES

LIST OF ABBREVIATIONS

CIS	Convective Ionospheric Storms
DMSP	Defense Meteorological Satellite Program
ESF	Equatorial Spread F
FAI	Field Aligned Irregularity
GPS	Global Positioning System
HWM	Horizontal Wind Model
IGRF	International Geomagnetic Reference Field
LT	Local Time
mex	MATLAB Executable
MSTID	Medium–Scale Traveling Ionospheric Disturbance
NRLMSISE–00	Naval Research Labs Mass Spectrometer, Incoherent Scatter (radar) Extended–2000
RTI	Rayleigh–Taylor Instability
SNR	Signal–to–Noise Ratio
TEC	Total Electron Content

CHAPTER 1

MOTIVATION

Within the past century, satellite communication has gone from non–existent to a common occurrence in everyday life. The signals of these communication systems must pass through thousands of kilometers of the Earth's atmosphere. One section of the atmosphere, the ionosphere, contains ionized gases which can modify radio signals as they pass through it. In fact, trans–ionospheric signals can be altered and degraded as a result of how the ionosphere behaves. This is a major issue for users who rely heavily on these signals. For example, the military puts forth a great amount of effort into ensuring their communication systems are robust to the ionosphere. Also, ionospheric turbulence can introduce large errors into GPS navigation systems, which, in addition to military use, have seen heavily utilization by civilians.

Societal dependence on these communication systems has motivated research in understanding and predicting Earth's dynamic atmosphere, and uncovering a plethora of information about this environment. One specific area of research that is of particular importance is ionospheric turbulence. The ionosphere is known to be very dynamic and can be disrupted due to a wide variety of causes. Significant research efforts have been carried out to study, characterize, and accurately predict ionospheric disturbances. Better prediction schemes of the disturbances lead to overall improvement of communication system design because knowledge of outages or degradation can benefit the user. Therefore, ionospheric research plays a crucial role in improving the reliability of satellite communication systems.

One type of ionospheric event is known as Equatorial Spread F (ESF). In a general sense, ESF describes ionospheric turbulence for regions near the equator. ESF often leads to plasma depletion in the ionosphere, also known as equatorial plasma bubbles (EPBs). This type of phenomena diffracts communication signals and decreases the signal integrity. ESF is commonly

attributed to the Rayleigh–Taylor instability (RTI) which describes the physical underlying process of how the instabilities develop.

Recently, there have been observations of mid–latitude events affecting ESF [1]. Another process, medium–scale traveling ionospheric disturbances (MSTIDs), have been observed to develop at mid–latitudes and propagate toward the equator. Once MSTIDs reach low latitudes, it is hypothesized that the MSTIDs can initiate or seed an ESF event there. The Perkins instability has been commonly referred to as the underlying mechanism to initiate MSTIDs [2].

In this thesis, the coupling of mid–latitude to equatorial events will be explored. The goal of this thesis is to use climatological modeling to investigate the claim of MSTIDs being a viable seed mechanism to ESF events. Climatological models will be run for both the RTI and Perkins instability. Data collected from the Christmas Island Radar observatory (CXI) will be analyzed for the RTI at an equatorial region. In addition, the Perkins instability will be analyzed for a mid–latitude location. It will be shown that Perkins instability will impact ESF events that the RTI does not predict.

Chapter 2 examines the characteristics of the ionosphere and introduces the climatological models used in the simulations. The instability mechanisms, the RTI and Perkins instability, are introduced in Chapter 3. Climatological models are used to study various components of the instability equations. Chapter 4 presents data from CXI, followed by simulations of the expected occurrence of the RTI for this location. In addition, the Perkins instability growth rate will be simulated for a mid–latitude location having the same longitude as CXI. The observed data and simulations will be compared. Finally, a conclusion of this work is presented in Chapter 5 along with a discussion of the future research topics that could be explored.

CHAPTER 2

INTRODUCTION

This chapter introduces basic information pertaining to the ionosphere. It provides necessary background and serves as a basis for more advanced topics discussed in this thesis.

2.1 The Ionosphere

The ionosphere is a very complex and coupled system and has inherent seasonalities, including yearly trends influenced by the Sun's solar cycle (with a period of approximately 11 years). There are also trends associated with the different seasons on Earth, as well as diurnal effects due to the production and loss of ions in the atmosphere as the Sun rises and sets. Magnetic field lines provide an avenue for plasma to travel and electric fields to propagate; hence regions at different latitudes can be coupled with one another. It is the goal of the ionospheric researcher to break down these complexities into simplified explanations of this dynamic, coupled, and overall complex system.

Earth's atmosphere can be divided into different regions. Generally, there are two conventions: one based on temperature corresponding to the neutral atmosphere, and another on plasma density corresponding to the ionosphere. Both are shown in Figure 2.1 along with commonly used names for the regions. Figure 2.2 shows the different compositions of the atmosphere. In the E and F regions, the O^+ density is the dominant ion species. This thesis is primarily concerned with instabilities generated at altitudes between 200 and 400 km where the plasma density increases and is maximum, known as the F layer.

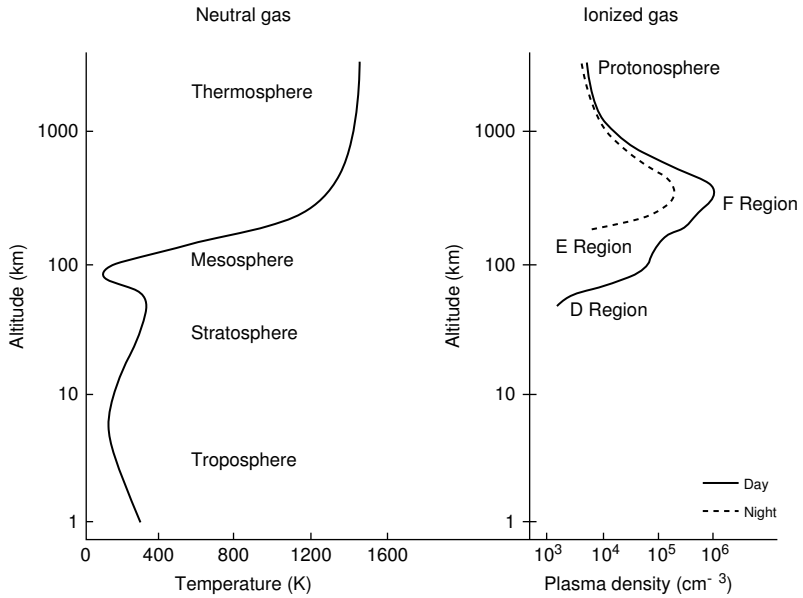

Figure 2.1: Classifications of regions of the atmosphere. After Kelley [3].

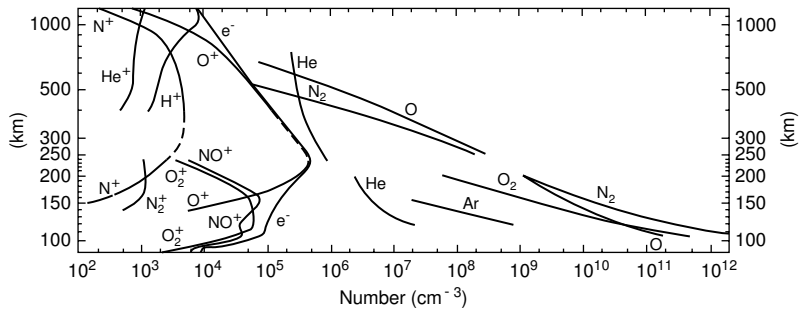

Figure 2.2: Density of various species of the atmosphere. After Kelley [3].

Table 2.1: Conductivities in the ionosphere.

	Type of Conductivity	Direction with respect to **B** and **E**
σ_P	Pedersen	$\perp \mathbf{B}, \parallel \mathbf{E}_\perp$
σ_H	Hall	$\perp \mathbf{B}, \perp \mathbf{E}$
σ_0	Specific	$\parallel \mathbf{B}$

2.2 Conductivities in the Ionosphere

In the ionosphere, the conductivity in Earth's atmosphere is known to be *anisotropic*, meaning that the electric field (**E**) and current (**J**) are in different directions. Therefore, the conductivity term is a tensor and the current is written as:

$$\mathbf{J} = \overleftrightarrow{\sigma} \cdot \mathbf{E} \tag{2.1}$$

where

$$\overleftrightarrow{\sigma} = \begin{bmatrix} \sigma_P & -\sigma_H & 0 \\ \sigma_H & \sigma_P & 0 \\ 0 & 0 & \sigma_0 \end{bmatrix} \tag{2.2}$$

The conductivities σ_P, σ_H, and σ_0 are known as the Pedersen, Hall, and specific conductivities, respectively. Figure 2.3 shows the direction of **J** given the directions of **B** and **E**. σ_P is the conductivity that is in the direction perpendicular to the magnetic field line and parallel to the perpendicular component of the electric field ($\perp \mathbf{B}, \parallel \mathbf{E}_\perp$). The conductivity σ_H is in the direction perpendicular to the magnetic field line and perpendicular to the electric field ($\perp \mathbf{B}, \perp \mathbf{E}$). Finally, σ_0 is the conductivity in the direction parallel to the magnetic field ($\parallel \mathbf{B}$). The conductivity descriptions are summarized in Table 2.1.

Equation 2.1 can be also written as

$$\mathbf{J} = \sigma_0 \mathbf{E}_\parallel + \sigma_P \mathbf{E}_\perp - \sigma_H \mathbf{E}_\perp \times \hat{z} \tag{2.3}$$

which shows explicitly what portions of the fields are affected by the Pedersen, Hall, and specific conductivities. The electric field in Equation 2.3 can be written to include the neutral wind term, **U**, by writing the total electric field as $\mathbf{E} + \mathbf{U} \times \mathbf{B}$ and Equation 2.3 then becomes [4]:

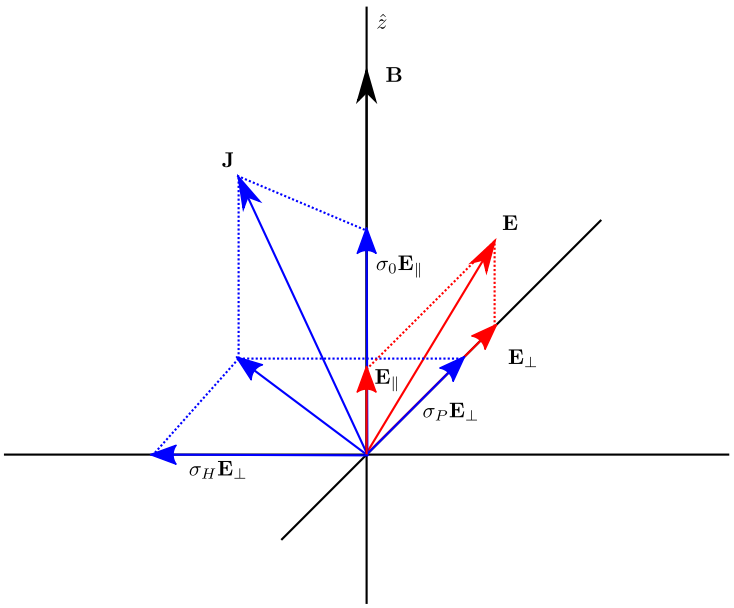

Figure 2.3: Diagram showing the relations of σ_P, σ_H, and σ_0. After http://wdc.kugi.kyoto-u.ac.jp/ionocond/exp/icexp.html.

$$\mathbf{J} = \sigma_0\mathbf{E}_\parallel + \sigma_P(\mathbf{E}_\perp + \mathbf{U}_\perp \times \mathbf{B}) - \sigma_H(\mathbf{E}_\perp + \mathbf{U}_\perp \times \mathbf{B}) \times \hat{z} \tag{2.4}$$

The conductivities can be written in terms of atmospheric parameters [3]:

$$\sigma_P = ne\left[\frac{b_i}{(1+\kappa_i^2)} - \frac{b_e}{(1+\kappa_e^2)}\right] \tag{2.5}$$

$$\sigma_H = \frac{ne}{B}\left[\frac{\kappa_e^2}{1+\kappa_e^2} - \frac{\kappa_i^2}{1+\kappa_i^2}\right] \tag{2.6}$$

$$\sigma_0 = ne(b_i - b_e) \tag{2.7}$$

Table 2.2 explains the terms used in the conductivity expressions. By using climatological models, the conductivities can be estimated for a given time and location. More information on the use of climatological models is found in Section 2.5.

A typical profile of the conductivities is found in Figure 2.4. The Pedersen conductivity is shown for both day and night. Notice that the conductivity along the magnetic field line, σ_0, is six orders of magnitude higher than σ_P and σ_H. This high conductivity allows for efficient mapping of electric fields along magnetic field lines [5]; it essentially makes the magnetic field lines act

Table 2.2: Terms used in conductivity expressions (Equations 2.5 – 2.7). *Note: j can refer either to an ion (i) particle or electron (e) particle.*

	Definition	Units
n	Electron Density	(# electrons)/ m^3
$q_e = e$	Fundamental Charge ($= q_i$)	C
b_j	Mobility $\left(= \frac{q_j}{M_j \nu_{jn}}\right)$	C · sec / kg
κ_j	Ratio of Gyrofrequency to Collision Frequency $\left(= \frac{q_j B}{M_j \nu_{jn}}\right)$	C · T · sec / kg
B	Magnetic Field Strength	T
M_j	Mass of Particle j	kg
ν_{jn}	Collision Frequency Between Particle j and Neutrals	(# collisions)/s

like equipotential lines.

2.3 Ionospheric Irregularities

There have been several names given to nighttime ionospheric irregularities at low latitudes in the research community, often given according to the type of instrument used to observe the storm. Historically and generically the term "Equatorial Spread *F*" (ESF) has been applied. This term comes from early observations of the low–latitude ionosphere using ionosondes because the returned signal's frequency or range was spread out due to the turbulent ionosphere [6].

Using radar instrumentation, the irregularities are often referred to as a plume, an example of which is shown in Figure 2.5. This figure shows the backscatter from a 50–MHz radar as a function of altitude and time for a low latitude location in Jicamarca, Peru. The plot shows irregularity regions rising and falling throughout the night; this particular example showcases the seemingly violent motion of plasma across hundreds of kilometers.

When imaging instrumentation is used, ionospheric instabilities are referred to as depletions or plasma bubbles. Optical instrumentation often uses the 630.0– and 777.4–nm airglow emission to observe depletions [8]. Imaging these emissions provides information about the ionosphere in two

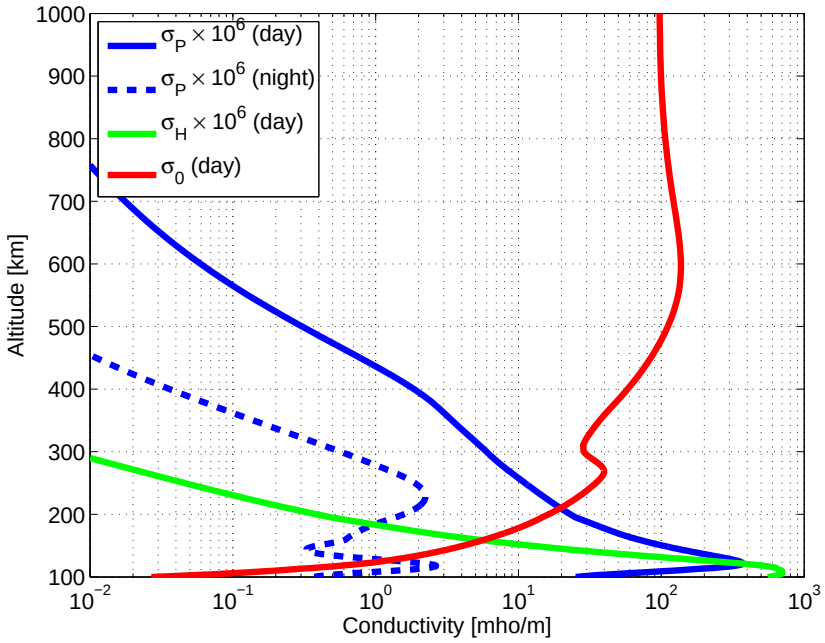

Figure 2.4: An example conductivity profile. Note the scaling of σ_P and σ_H and the relatively large conductivity of σ_0.

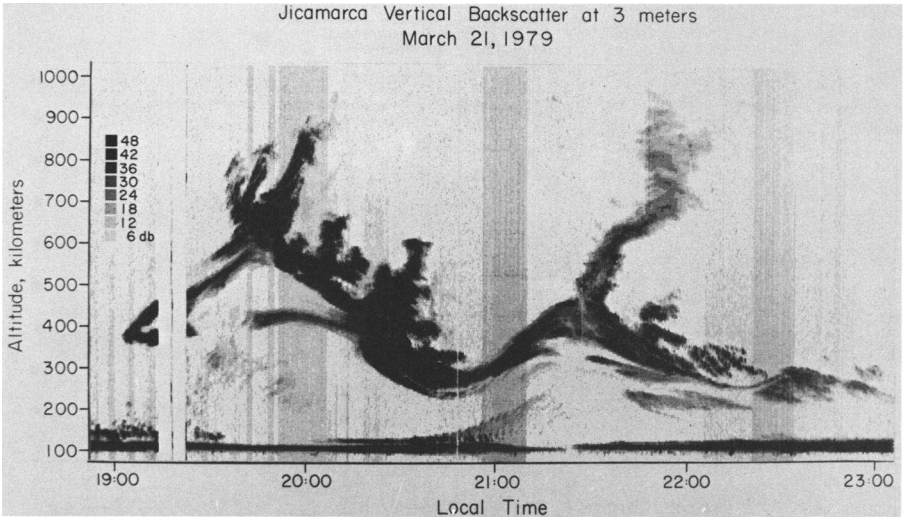

Figure 2.5: Example range–time intensity map for radar backscatter at Jicamarca, Peru. After Kelley et al. [7].

spatial dimensions and as a function of time.

At mid–latitudes, the development of ionospheric irregularities are physically different due in part to the finite dip angle of the magnetic field. Nighttime mid–latitude structures, or medium–scale traveling ionospheric disturbances (MSTIDs), are characterized by bands of plasma density variation and propagate toward the equator. Ground–based imaging equipment has been used to observe the bands [9]. Also, a dense network of about 1000 dual–frequency GPS receivers has been used to measure the total electron content (TEC) fluctuations of MSTIDs in Japan [10]. More information on EPBs and MSTIDs is given in the next section along with example images and statistics of the structures.

2.4 Observations

There has been a rich history of observing ionospheric irregularities, and many data sets have been compiled over the years. This section will give examples of data collected at both equatorial and mid–latitude locations and compare and contrast the observations of the two regions. Also, statistical information of the collected data will be given for the two regions.

2.4.1 Equatorial

At equatorial regions, ionospheric instabilities (also known as ESF) are often observed to be field aligned irregularities (FAIs), meaning that the structure of electron density depletions (or EPBs) is extended along the magnetic field line. Figure 2.6 contains images that display these EPBs at various field sites near the equator. The dark portions of the images are where the electron density is depleted. ESF structures tend to drift from west to east. Notice that the depletions can bifurcate and branch out to form additional structure irregularities as in Figure 2.6c.

Figure 2.6a displays another feature of FAIs often seen in observations: the bands can be periodic. It is hypothesized that this periodicity is from an initiation of ESF due to atmospheric gravity waves [11]. However, not all structures have periodicity.

The plasma density of the ionosphere can be measured by satellites. One

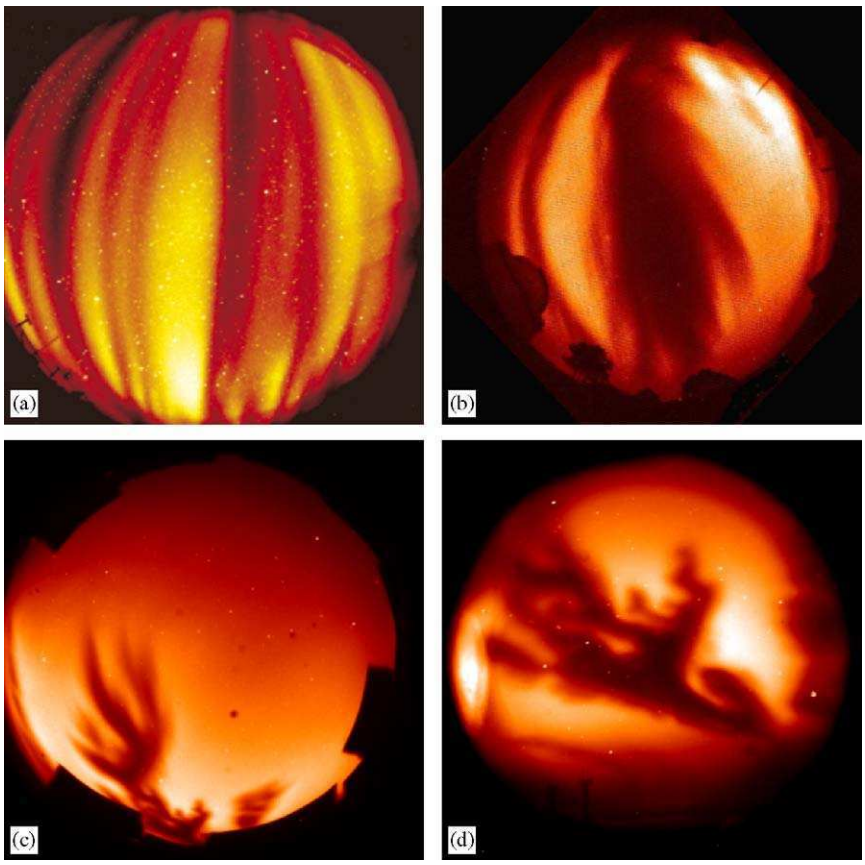

Figure 2.6: Example images of ionospheric irregularities near the equator using all–sky imagers. (a) Christmas Island, (b) Brazapolis, Brazil, (c) Haleakala, Hawaii (viewing poleward), and (d) Haleakala, Hawaii (viewing along magnetic field lines). After Makela [8].

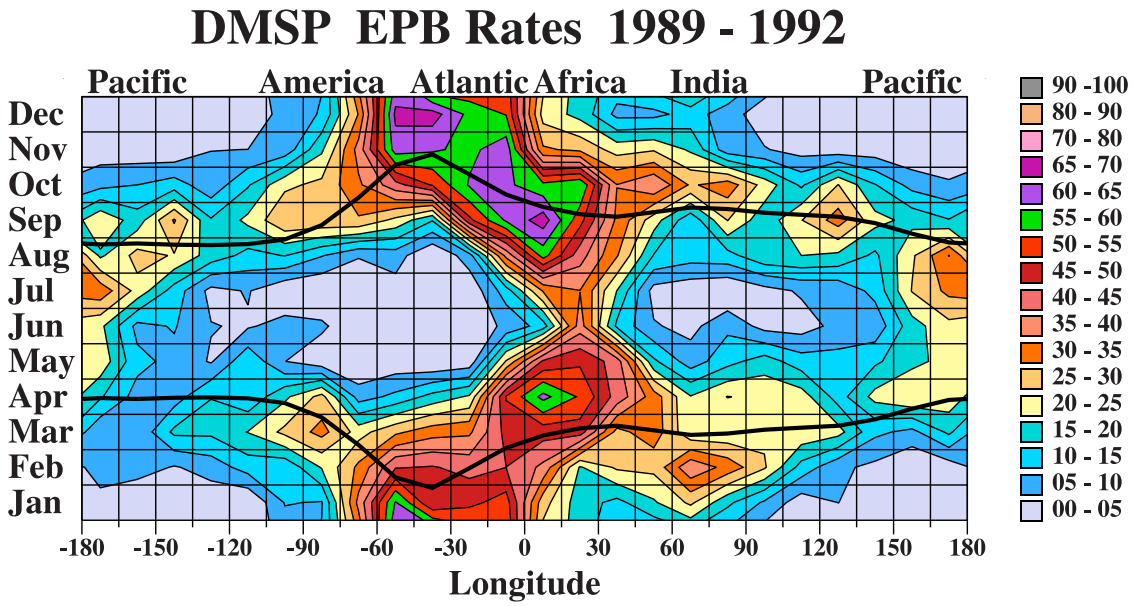

Figure 2.7: Occurrence rates of EPBs as measured by the DMSP satellite, solar maximum years. After Gentile et al. [12].

particular satellite, the Defense Meteorological Satellite Program (DMSP) spacecraft has been used for long–term climatological studies of the EPB occurrence [12]. Using Special Sensor–Ions, Electrons, and Scintillation (SSIES) instruments, the DMSP satellite measures the electron density for various longitudes in a Sun–synchronous, polar orbit at an altitude of ∼840 km with an inclination of 98.7°.

Sample results of a DMSP study are shown in Figures 2.7 and 2.8 for years corresponding to solar maximum and solar minimum years, respectively. The EPB rates are defined as the ratio between the number of EPB detections to the total number of orbits for a given month. The data were grouped into 15° longitudinal bins.

There is a clear correlation between solar activity and occurrence statistics of EPBs measured by the DMSP satellites. Figures 2.7 and 2.8 also show the longitudinal dependence of EPBs as well as monthly seasonalities. The solid black line in the figures represent where the magnetic longitudinal declination angle lines up with the solar terminator. Section 3.2.1 discusses how this affects occurrence rates of EPBs.

There have also been long–term studies using optical imagers. Figure 2.9 shows data from a study using the Cornell Narrow Field Imager (CNFI), located at Mount Haleakala, Hawaii. Here, the data from the imagers were

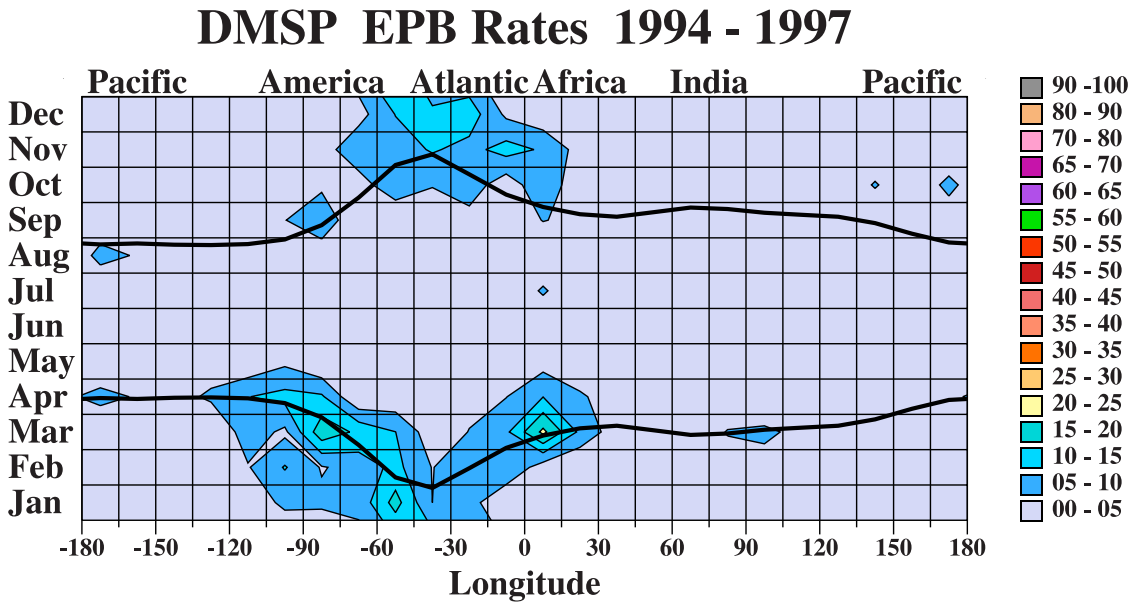

Figure 2.8: Occurrence rates of EPBs as measured by the DMSP satellite, solar minimum years. After Gentile et al. [12].

classified as a binary depletion/no depletion and sorted into 15–minute bins. The occurrence rate is defined as the ratio between depletions to the total number of usable observations (some data could not be included due to instrument maintenance and moonlight contamination). The corresponding $F_{10.7}$ and K_p values are also given. This figure gives the statistical rates of EPB development as a function of LT throughout the night and also as a function of day of the year.

Notice the shift of occurrence rate into later parts of the night as the days progress into solar minimum years. The DMSP data do not reflect these EPB occurrences. Since the Sun–synchronous DMSP satellite does not take measurements in a region for early morning times, the satellite instrumentation does not detect those EPBs developed during this period [13].

2.4.2 Mid–Latitude

There have also been studies of irregularity structure at mid–latitudes which are known as medium–scale traveling ionospheric disturbances (MSTIDs). Like ESF, MSTIDs are an example of an instability in the nighttime ionosphere. However, MSTIDs are mid–latitude phenomenon characterized by

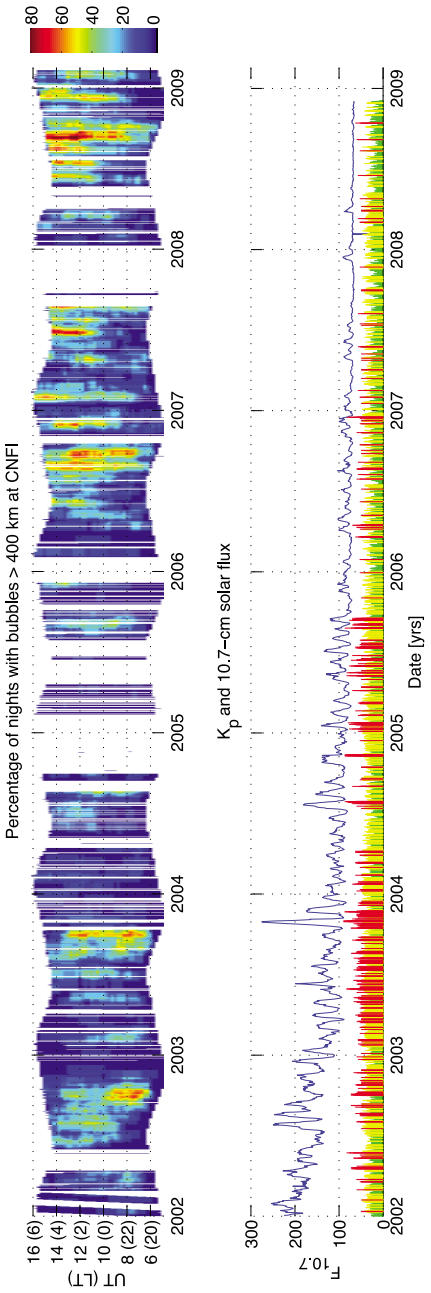

Figure 2.9: (top) Occurrence statistics of EPBs as measured by an optical imager. (bottom) Corresponding $F_{10.7}$ and K_p values. After Miller et al. [13].

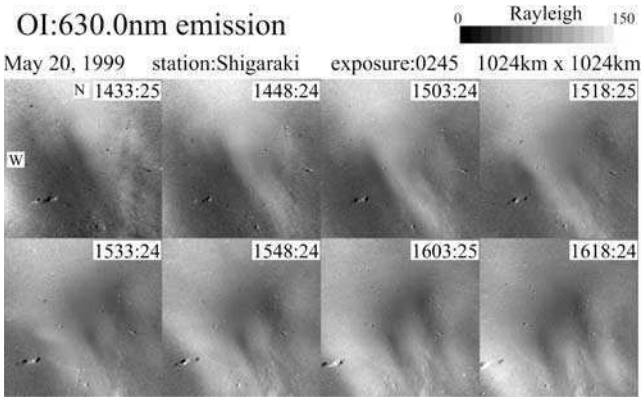

Figure 2.10: Example time sequence images of MSTIDs propagating. After Shiokawa et al. [14].

differing bands of conductivity with periods of 1 to 2 hours and wavelengths between 50 and 500 km. The most notable observational differences between MSTIDs and ESF are their alignment, propagation direction, and region of occurrence. In the northern hemisphere, MSTIDs travel southwest and are aligned from northwest to southeast. Also, MSTIDs primarily occur during solar minimum years near the December and June solstice [14]. Figure 2.10 shows an example time sequence of MSTIDs as they propagate in the southwest direction at Shigaraki, Japan. The images were taken using an all–sky imaging system looking at the 630.0–nm red–line emission.

Figure 2.11 shows a compass plot of the wavefront direction and velocities of the recorded MSTIDs from Arecibo, Puerto Rico. This figure shows the tendency of MSTIDs to propagate in the southwest direction for a northern hemisphere location. These phase fronts agree with the orientation of the band structure of Figure 2.10.

Statistical studies of MSTIDs have also been conducted [14, 15]. Figure 2.12 shows MSTID occurrence rates, emphasizing that MSTIDs occur more frequently during low solar activity (b) than high solar activity (a). Also, MSTIDs have a higher rate of occurrence for nights near the June and December solstice, with a higher preference toward the June solstice.

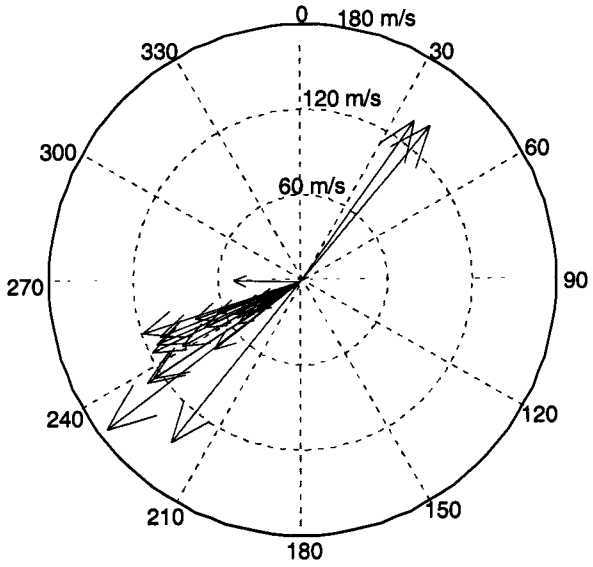

Figure 2.11: A compass plot of the directions and velocities of recorded MSTIDs. After Garcia et al. [15].

2.5 Climatological Models

In this thesis, several simulations of the instability mechanisms that create ionospheric irregularities are carried out through the use of climatological models. These simulations require temperature, species density, magnetic field strength, and wind information for the upper atmosphere. Climatological models are based on historical data and take into account daily, monthly, and yearly seasonalities. Hence, the parameters provided by climatological models are not necessarily the exact values, but rather a best guess at the typical value of a parameter given the location, time of day, day of the year, and solar cycle. Climatological models are analogous to almanacs; they provide an estimate into the future based on history.

Models estimate the value of a parameter. To emphasize this point, Figures 2.13 and 2.14 give two example comparisons of observed and modeled data. Figure 2.13 gives an example of good agreement, while Figure 2.14 shows disagreement. The top portions of the figures give total electron content (TEC) as a function of time and day as measured by a dual–frequency GPS receiver in Sangre Grande, Trinidad. From the GPS receiver, the satellite location can be obtained, and by using the climatological model, the electron density can be estimated along the path from the receiver to the satellite.

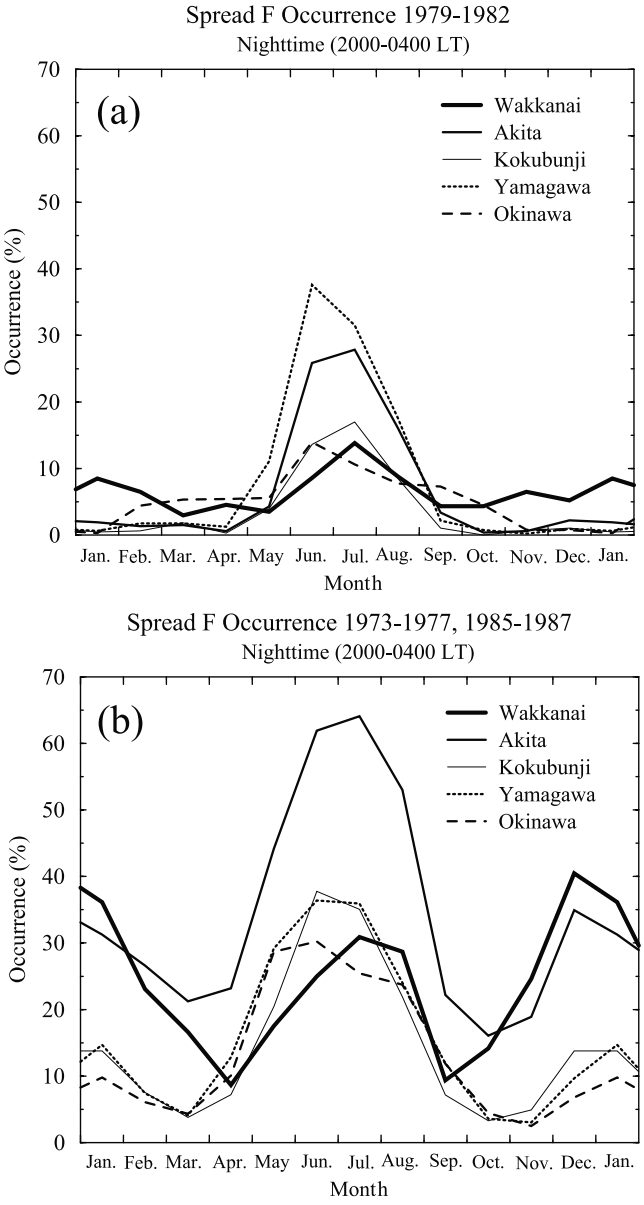

Figure 2.12: Occurrence statistics of ionospheric irregularities for several sites in the Japanese sector for both (a) high solar activity and (b) low solar activity. After Shiokawa et al. [14].

Table 2.3: Climatological models used for growth rate models.

Rayleigh–Taylor Growth Rate Model		
Term	**Explanation**	**Model Used**
Σ_P^F, Σ_P^E	Integrated Pedersen conductivity	IGRF, IRI, MSIS
N	Integrated electron density	IGRF, IRI
$\frac{\mathbf{E}\times\mathbf{B}}{\lvert\mathbf{B}\rvert^2}$	E cross B drift	Fejer drift
ν_{eff}^F	Effective ion–neutral collision frequency	IGRF, IRI, MSIS
U_m	Meridional wind	HWM
Perkins Instability Growth Rate Model		
Term	**Explanation**	**Model Used**
D	Dip angle	IGRF
B	Magnetic field strength	IGRF
H_n	Neutral scale height	MSIS
$\mathbf{U}_0$	Background wind	HWM
$\mathbf{E}_0$	Background electric field	Fejer drift, IGRF

Integrating the electron density along this path results in the modeled TEC value (bottom portions of the figures). The discrepancies are hypothesized to be the result of ionospheric irregularities, which the climatological model does not predict.

In total, five climatological models are used for the simulations conducted in this thesis. The Naval Research Labs Mass Spectrometer, Incoherent Scatter (radar) Extended–2000 (NRLMSISE–00) [16] supplies the density of neutral parameters. The International Reference Ionosphere 2007 (IRI07) [17] provides estimates of the plasma densities and temperatures. The Horizontal Wind Model 2007 (HWM07) [18] models the meridional and zonal component of the neutral winds. The Fejer drift model [19] is used to estimate the $\mathbf{E} \times \mathbf{B}$ drift at equatorial regions. Finally, the International Geomagnetic Reference Field (IGRF) [20] model contains information about the direction and magnitude of the magnetic field line for a given time and location.

The models created in this thesis to simulate the occurrence of ionospheric irregularities use the prescribed climatological models. Table 2.3 explains the terms used in these models (Rayleigh-Taylor growth rate and the Perkins instability growth rate) and the respective climatological model used to estimate each term. Chapter 3 discusses the growth rate models in detail.

With the exception of Fejer drift, these models are written as FORTRAN functions. In order to use these models within the MATLAB programming

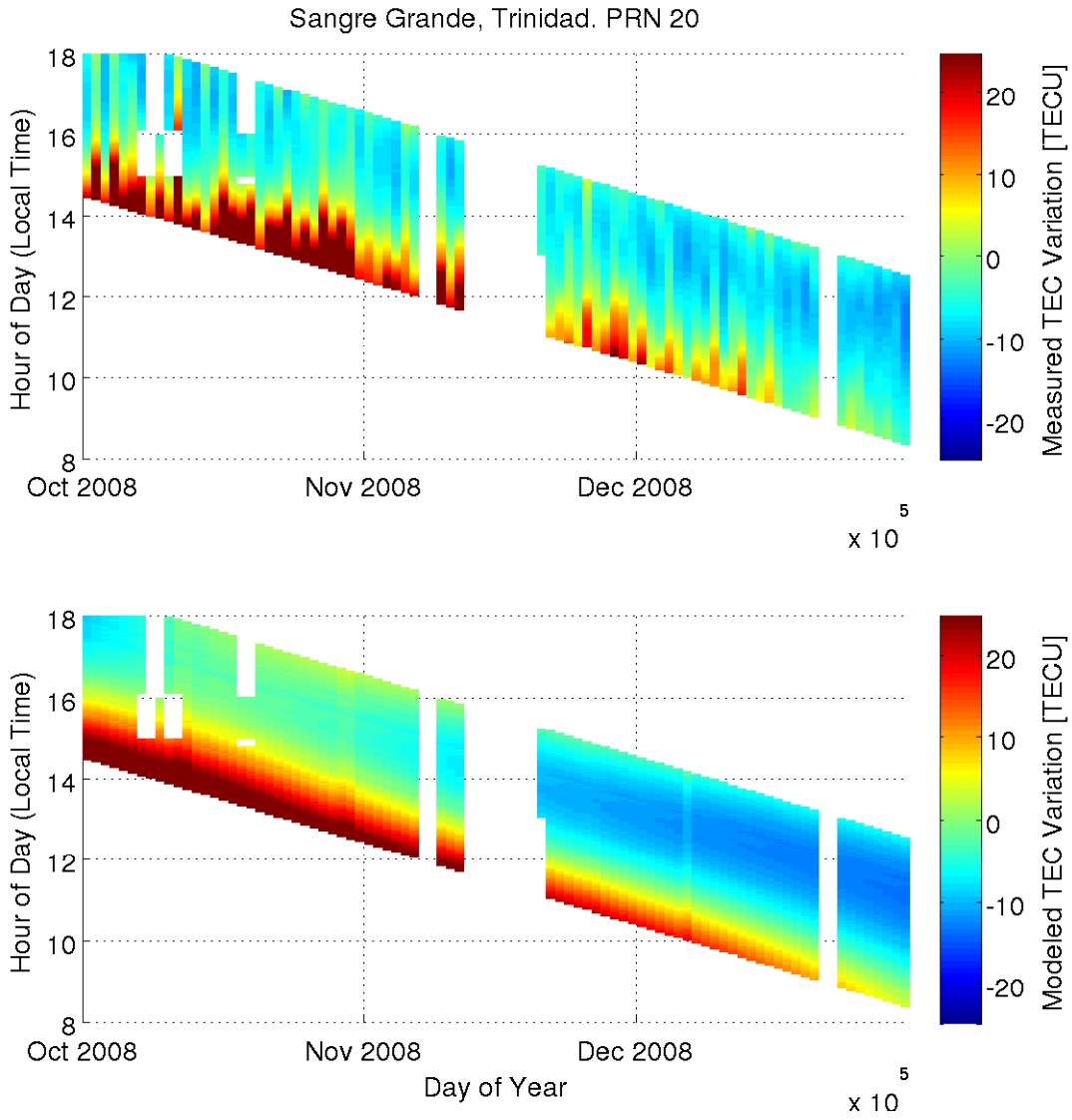

Figure 2.13: A comparison of the observed TEC (top) with the climatological model IRI (bottom), year 2008. In general, there is good agreement between the observed and modeled data.

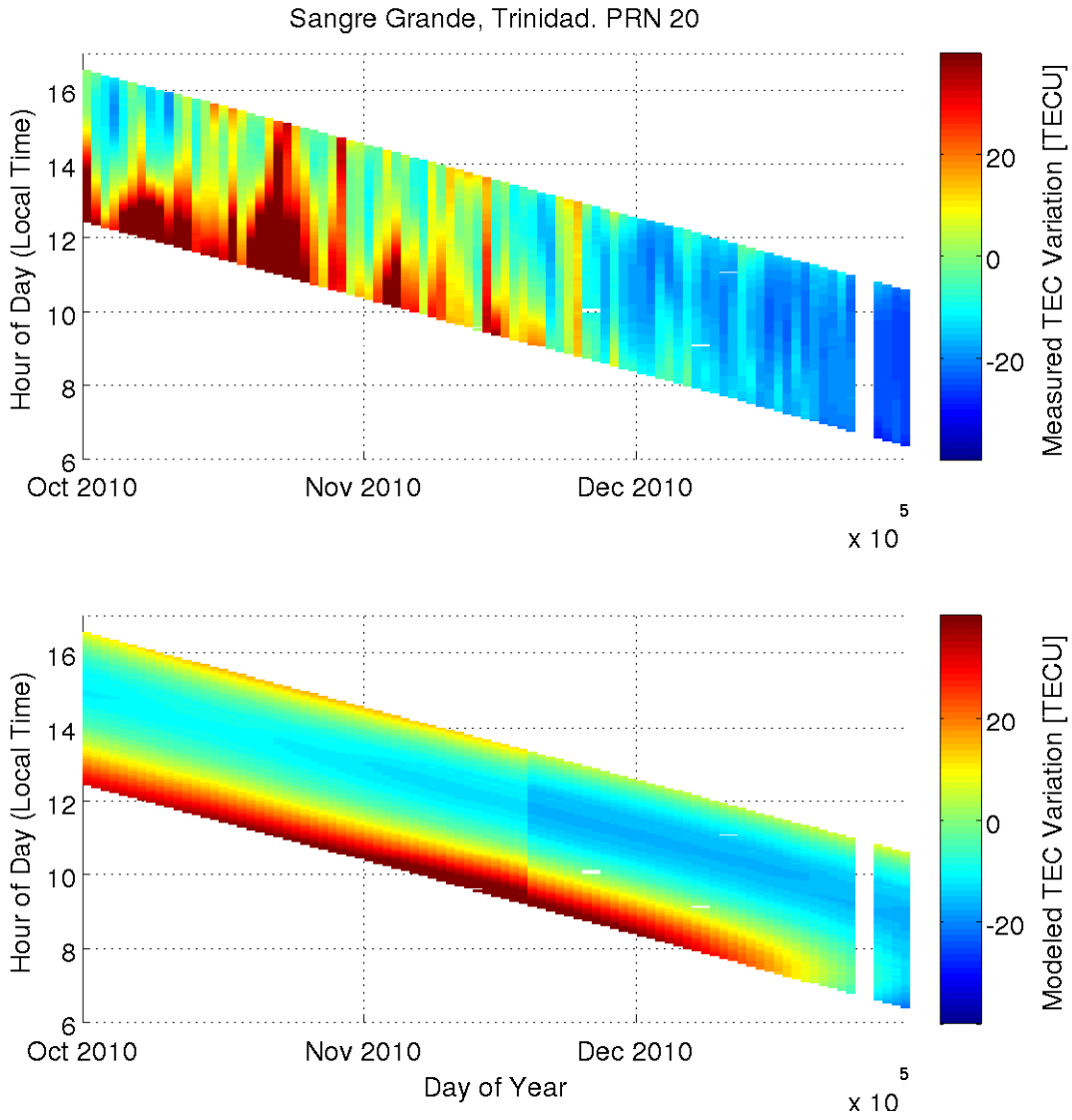

Figure 2.14: A comparison of the observed TEC (top) with the climatological model IRI (bottom), year 2010. Here the model does not predict the large fluctuations of the observed TEC.

language, MATLAB executable (mex) wrappers are created to run the FORTRAN code. The mex functions take advantage of the high–level language of the MATLAB environment in combination with the efficient FORTRAN functions.

2.6 Conclusion

In this chapter, basic information about the composition of the ionosphere is given. The ionosphere is a very dynamic system, and instability mechanisms are used to explain small–scale structures that can develop. Example images of the structures are given for sites at equatorial and mid–latitude regions and are compared. Climatological models were introduced as a foundation for more complex instability models that will be developed in Chapter 3. In the next chapter, the instability mechanisms will be further explored in order to create a model of ionospheric instabilities at low and mid–latitudes.

CHAPTER 3

INSTABILITY MECHANISMS

In this thesis, two instability ionospheric mechanisms will be explored. The Rayleigh–Taylor instability describes the development of plasma instabilities near equatorial latitudes while the Perkins instability describes events at mid–latitudes. The Rayleigh–Taylor instability was proposed as a mechanism for the development of equatorial irregularities by Dungey in 1956 [21]. The Perkins instability was developed by Perkins in 1973 [2] to describe nighttime structures in the mid–latitude ionosphere.

3.1 The Rayleigh–Taylor Instability

In the most general sense, a Rayleigh–Taylor instability (RTI) describes an instability between two fluids of different densities with the heavier fluid above the lighter. With a perturbation at the interface, the light fluid will rise and the heavy fluid will sink, causing the system to go unstable while the two fluids interchange. Within the context of the ionosphere, the heavy fluid involved in the RTI is the dense plasma in the nighttime F region, and the light fluid is analogous to the region below the F layer where the plasma density is less. The heavy fluid is supported against gravity by the magnetic field lines, explaining why the instability is active near the magnetic equator where the magnetic field, $\mathbf{B}$, is horizontal. At locations poleward of the magnetic equator where there is a finite dip angle, gravity pulls plasma along the magnetic field lines.

The RTI is illustrated in Figure 3.1. In this diagram, gravity is downward and the northward $\mathbf{B}$ is into the page. This cartoon simplifies the ionosphere into two distinct regions: a dense plasma above (shown as diagonal lines) with zero plasma density below. In other words, there is a sharp upward gradient of electrons at the interface between regions n_2 and n_1. A small

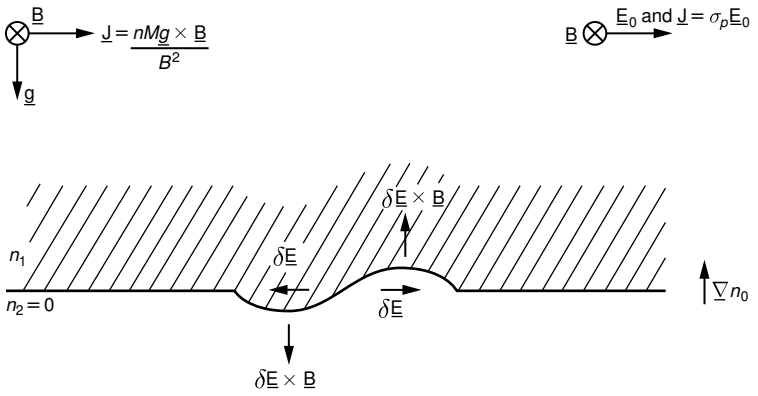

Figure 3.1: A cartoon of the Rayleigh–Taylor instability. After Kelley [3].

perturbation causes a fluctuation of density at the interface. This creates small electric fields, $\delta\mathbf{E}$, due to gravitational current because of the difference in density. Using the right–hand rule, a force is created, $\delta\mathbf{E} \times \mathbf{B}$, which is downward for $\delta\mathbf{E}$ pointing to the west, and upward for $\delta\mathbf{E}$ pointing to the east. This creates an even larger displacement, the process is repeated, and the system goes unstable. A sketch of this instability as a time sequence is shown in Figure 3.2. These snapshots represent the plasma "bubbles" of the ionosphere, characterized by the depletions of plasma density.

Radar instrumentation can be used to detect plasma bubbles. The Bragg wavelength of a radar beam dictates the minimum size of the irregularity that can be detected. For example, at Jicamarca, a 50–MHz radar beam is used to probe the ionosphere. The returns detect 3–m (corresponding to the Bragg wavelength) irregularities of the ionosphere and are able to record the temporal variations of the plasma irregularities for a given altitude range.

3.2 RTI Growth Rate

Growth rates of an instability process describe how fast an instability grows or decays. A growth rate has the units "e–folds per second"; it accounts for how many e–folds a wave will grow per unit time (or for the case of negative growth rates, how many e–folds the wave will dampen per unit time). In the standard plane wave equation, $e^{j(\mathbf{k}\cdot\mathbf{r}-\omega t)}e^{\gamma}$, the growth rate is the γ term. In ionospheric research, the growth rate is a good indicator of how likely an irregularity event could occur: high growth rates reflect high probabilities of

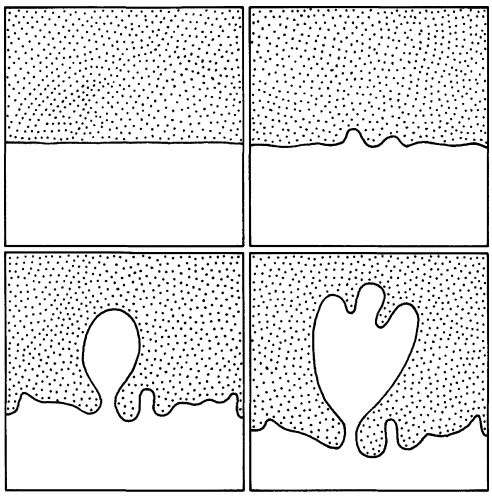

Figure 3.2: Example of the Rayleigh–Taylor instability process as a function of time. The system goes unstable with a seed perturbation. After Kelley [3].

irregularity development while low growth corresponds to a dampening of an instability process.

Following Martinis [22], the linear growth rate for the Rayleigh–Taylor instability is given as

$$\gamma_{RT} = \frac{\Sigma_P^F}{\Sigma_P^E + \Sigma_P^F} \cdot \frac{\nabla N}{N} \cdot \left[\frac{\mathbf{E} \times \mathbf{B}}{|\mathbf{B}|^2} - \frac{\vec{g}}{\nu_{eff}^F} - \mathbf{U}_m \right] \tag{3.1}$$

Parameters along with their respective units are listed in Table 3.1. Note that Σ_P^F, Σ_P^E, and N are magnetic field line integrated quantities and are written as

$$\Sigma_P^F = \int\limits_{z \,\in\, F\text{–region}} \sigma_P \; dz \tag{3.2}$$

$$\Sigma_P^E = \int\limits_{z \,\in\, E\text{–region}} \sigma_P \; dz \tag{3.3}$$

$$N = \int n \; dz \tag{3.4}$$

where σ_P is the Pedersen conductivity, n is the electron density, and dz is the path along the magnetic field line. The altitude choices for the E and F regions are chosen based on the profile of the electron density. The lower limit of integration was selected to be 90 km. The effective ion–neutral collision

Table 3.1: Terms of the Rayleigh–Taylor growth rate.

	Definition	Units
Σ_P^F	Integrated Pedersen conductivity in the F region	mhos
Σ_P^E	Integrated Pedersen conductivity in the E region	mhos
N	Integrated electron density	(# electrons)/ m^3
$\mathbf{E}$	Electric field	V/m
$\mathbf{B}$	Magnetic field	T
$\vec{g}$	Acceleration due to gravity	m/s^2
ν_{eff}^F	Effective ion–neutral collision frequency in the F region	(# collisions)/s
$\mathbf{U}_m$	Meridional neutral wind	m/s

frequency, ν_{eff}^F, is also a field–line integrated quantity defined as [23]

$$\nu_{eff}^F = \frac{\int_b^t n\nu_{in}\ dz}{\int_b^t n\ dz} \tag{3.5}$$

where ν_{in} is the ion–neutral collision frequency, and b and t are the bottom–side and topside altitudes of the F region, respectively.

What follows is a brief explanation of each term in Equation 3.1 along with an example plot of altitude versus local time of the term over a night. Finally, an example plot will be shown that gives the total Rayleigh–Taylor growth rate for a night.

3.2.1 $\Sigma_P^F/(\Sigma_P^E + \Sigma_P^F)$

The first term in Equation 3.1 is a ratio between the integrated Pedersen conductivity in the F region and to that in the total E and F regions. This term maximizes to 1 when there is zero integrated Pedersen conductivity in the E region. The Pedersen conductivity is the conductivity of the anisotropic ionosphere in the direction that is perpendicular to the magnetic field line and parallel to the portion of the electric field that is perpendicular to the magnetic field line ($\sigma_P \rightarrow\perp \mathbf{B}$ and $\parallel \mathbf{E}_\perp$).

Physically, this ratio term can be explained as follows: for a particular

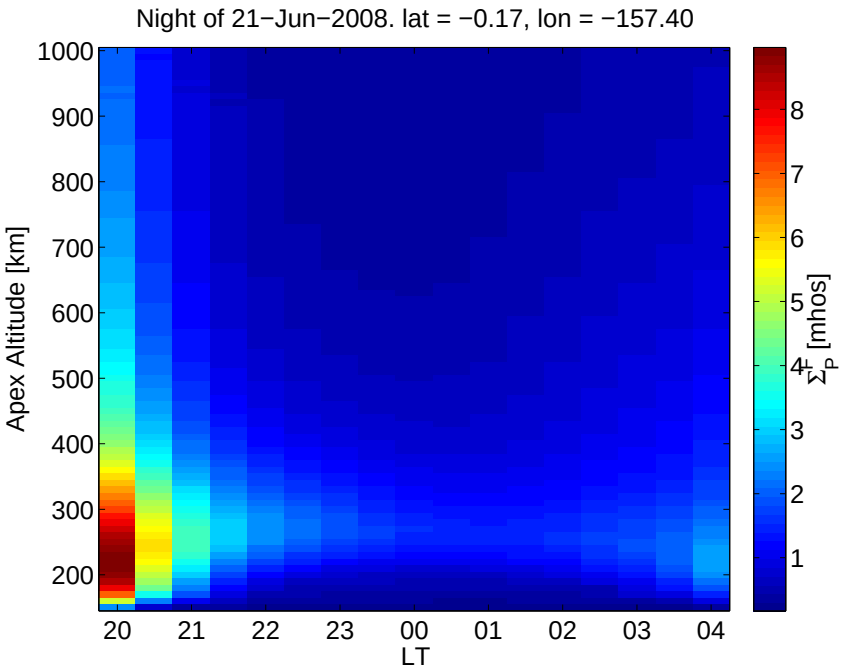

Figure 3.3: An example of the Σ_P^F as a function of apex altitude and time.

region, as the sun sets, plasma in the E region will recombine first because of the higher neutral density at lower altitudes, thereby having higher recombination rates. If the sunset terminator exactly lines up with the magnetic longitude of the location, there will be high resistance between magnetic field lines in both of the E regions. Therefore, the F region will support an electric field. If, on the other hand, the sunset terminator does not line up with the magnetic longitude, the Pedersen conductivity will be finite for a portion of the magnetic field line in one of the E regions and electric fields can be shorted out to lower altitudes, thus inhibiting the Rayleigh–Taylor instability. Tsunoda [24] did a complete analysis of this phenomena for varying locations that have different declination angles for several magnetic longitude locations. The general longitudinal seasonal occurrence of ESF appears to follow this hypothesis [12].

An example of Σ_P^F for a night during solar minimum at an equatorial location is given in Figure 3.3. Likewise, Σ_P^E is shown in Figure 3.4 and the corresponding ratio, $\Sigma_P^F/(\Sigma_P^E + \Sigma_P^F)$, is given in Figure 3.5. This ratio favors RTI for early times of the night. After local midnight, the term decreases, which is expected since the plasma further recombines after midnight.

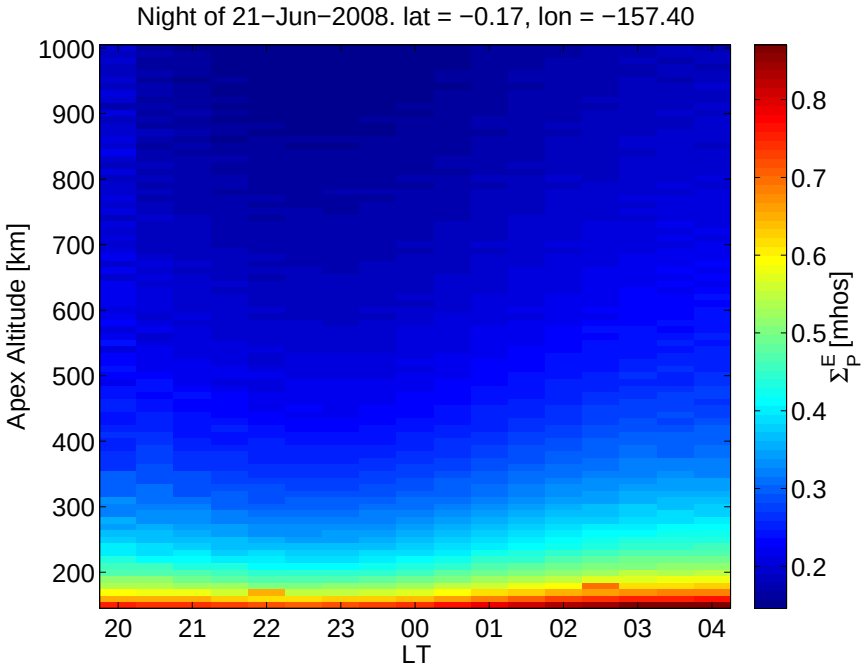

Figure 3.4: An example of the Σ_P^E as a function of apex altitude and time.

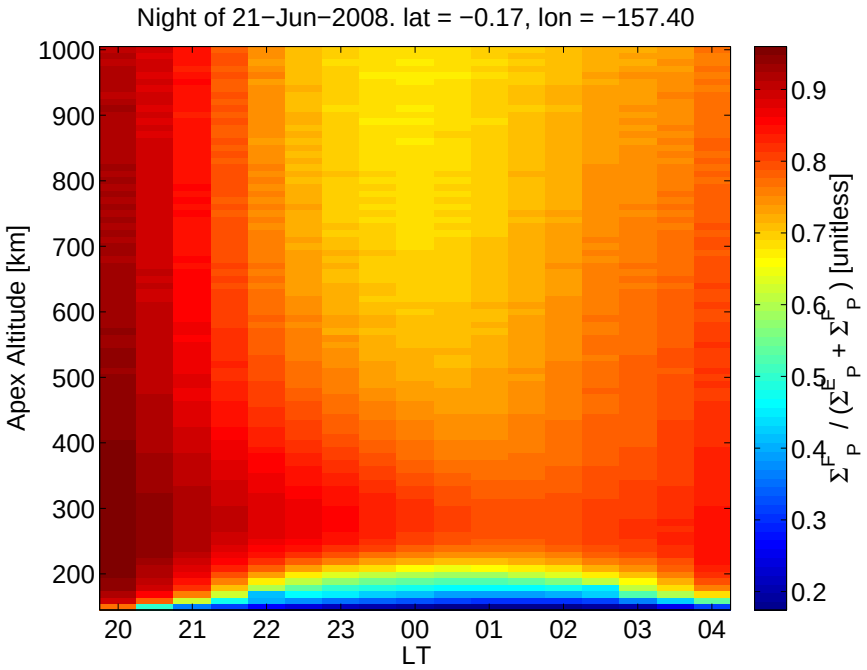

Figure 3.5: The ratio $\Sigma_P^F/(\Sigma_P^E + \Sigma_P^F)$ as a function of apex altitude and time. The term decreases after local midnight.

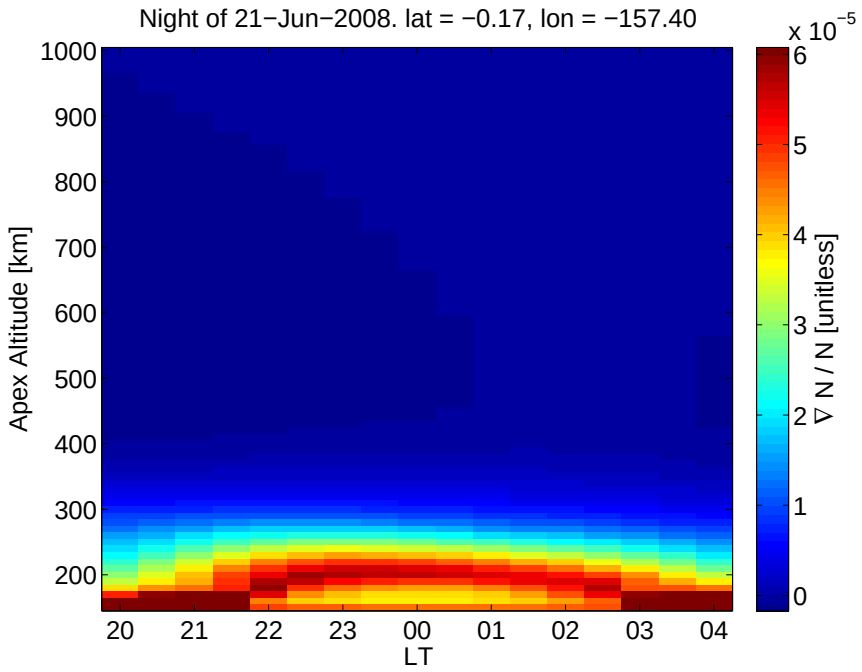

Figure 3.6: An example of the normalized integrated electron density gradient.

3.2.2 $\nabla N/N$

Figure 3.6 shows an example of the gradient of electron density. Essentially, $\nabla N/N$ captures the location of the bottomside of the F region. This region is most susceptible to instabilities because it represents the interface from low to high electron density (see Figure 3.1). As indicated by Equation 3.1, the steeper the gradient, the stronger the growth rate. Hence, the growth rate is enhanced at these areas. For reference, an example profile of the local electron density is shown in Figure 3.7. Also shown in Figure 3.8 is the integrated electron density N profile. Notice that the peak in the integrated electron density is higher in altitude than the local density because through the magnetic field lines the integrated term includes the density of the F region.

3.2.3 $(\mathbf{E} \times \mathbf{B})/|\mathbf{B}|^2$

The next three terms ($(\mathbf{E} \times \mathbf{B})/|\mathbf{B}|^2$, $\vec{g}/\nu_{eff}^F$, and $\mathbf{U}_n$) are all motion terms (all having units [m/s]). Large upward motion terms increase the Rayleigh–

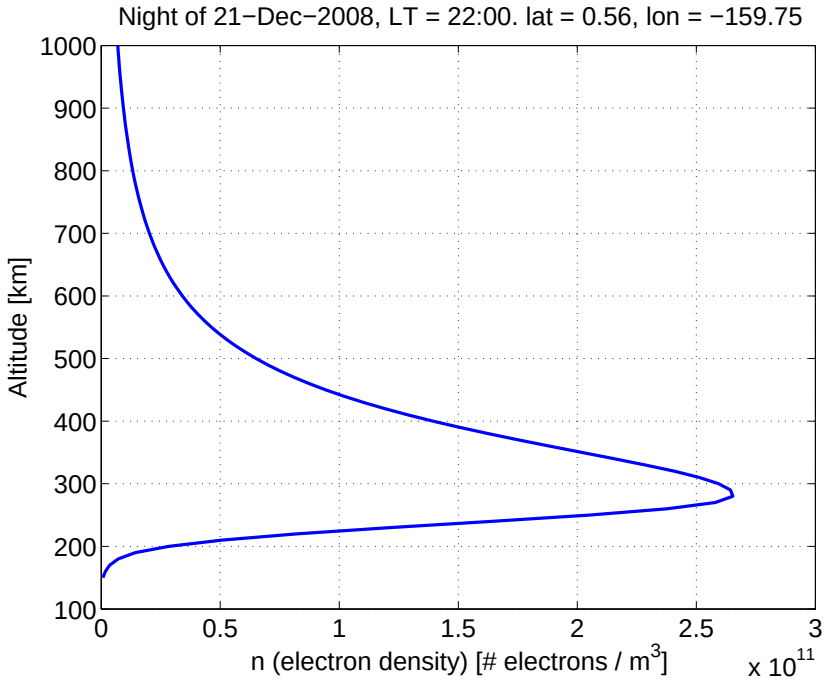

Figure 3.7: An example profile of the local electron density.

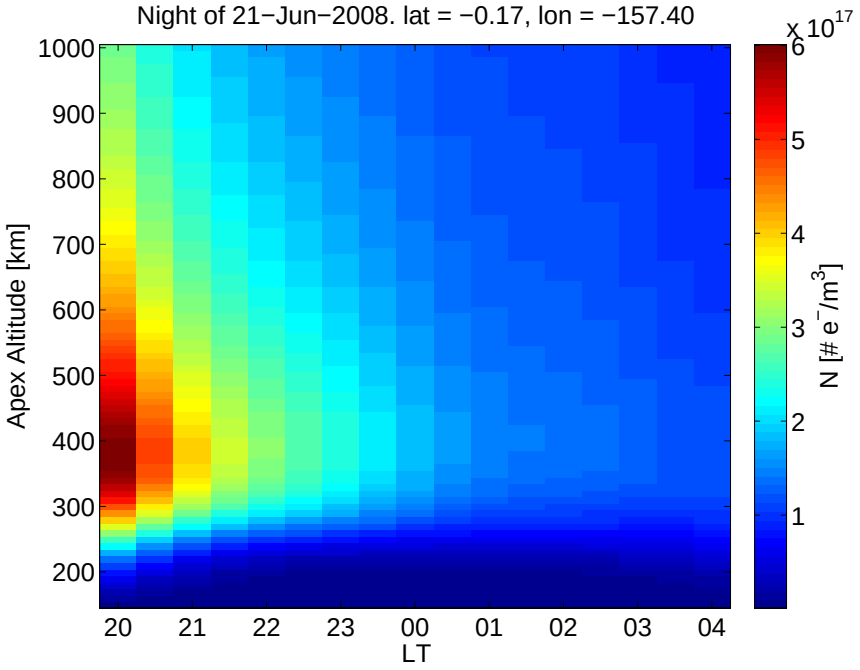

Figure 3.8: An example profile of the integrated electron density N.

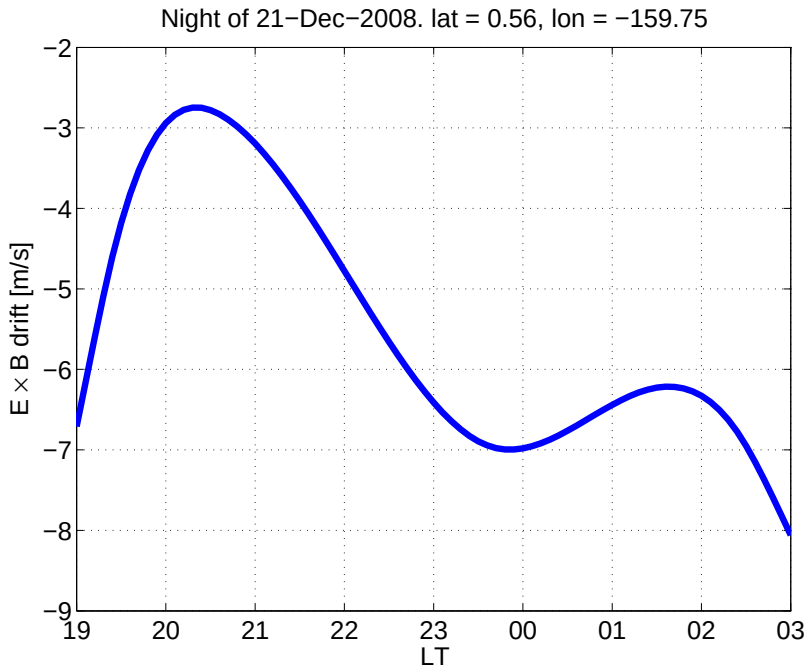

Figure 3.9: An example $\mathbf{E} \times \mathbf{B}$ drift during the night at an equatorial location. Note that the Scherliess and Fejer model does not include altitude dependence in the calculation of the drift value.

Taylor growth rate. The first term is called the "E Cross B drift" which is derived from the balance of the Lorentz force:

$$\mathbf{F} = m\frac{d\mathbf{v}}{dt} = q(\mathbf{E} + \mathbf{U} \times \mathbf{B}). \tag{3.6}$$

The solution to this equation is given as:

$$\mathbf{v} = \frac{\mathbf{E} \times \mathbf{B}}{|\mathbf{B}|^2} \tag{3.7}$$

and is valid for both ions and electrons.

The $\mathbf{E} \times \mathbf{B}$ drift is modeled after Scherliess and Fejer [19]. This model is valid for magnetic equatorial regions (which is where the source of the data from the model derivation) and uses cubic–B spline functions to interpolate the vertical drifts. Figure 3.9 shows an example profile of the $\mathbf{E} \times \mathbf{B}$ drift for a night. The drifts from this model are assumed to be constant over the E and F region altitudes (200–400 km).

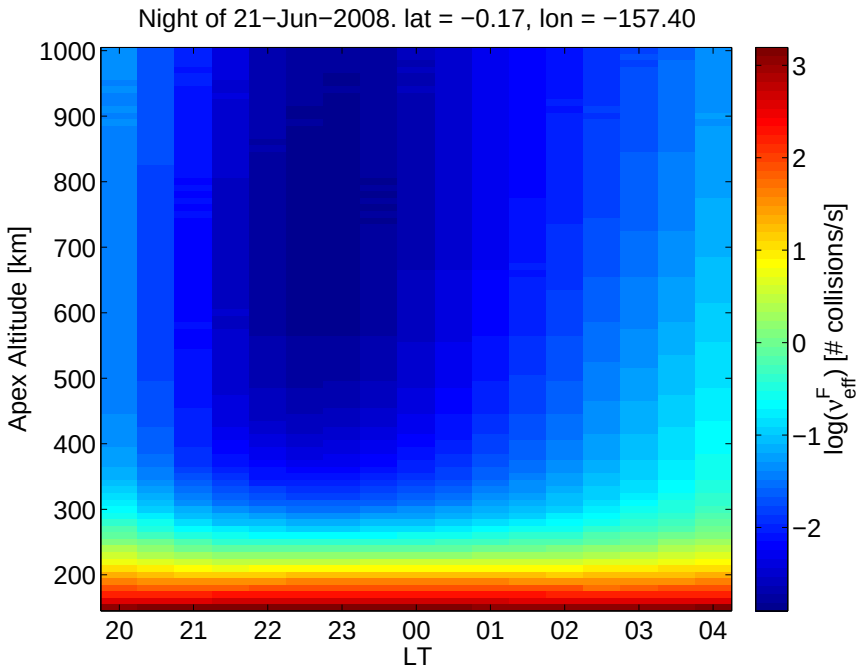

Figure 3.10: The effective ion–neutral collision frequency, ν_{eff}^F. Note that ν_{eff}^F is on a log scale.

3.2.4 $\vec{g}/\nu_{eff}^F$

The second motion term is a function of ν_{eff}^F, which was defined in Equation 3.5. Figure 3.10 shows ν_{eff}^F as a function of local time and altitude, and Figure 3.11 displays the complete additive motion term $-\vec{g}/\nu_{eff}^F$. This term favors the growth rate at high altitudes just before local midnight. However, as seen in Section 3.2.2, the multiplicative gradient term ($\nabla N/N$) is negative at these high altitudes, therefore inhibiting the growth rate there.

3.2.5 $\mathbf{U}_m$

The last motion term in Equation 3.1 is the meridional component of the neutral wind, obtained from HWM 07 [18]. An example of the meridional wind profile is displayed in Figure 3.12. The meridional wind physically pushes the plasma density distribution. It can also transport plasma across hemispheres, leading to an uneven density distribution across field lines [25]. This imbalance changes the field line integrated quantities, which then affects the growth rate of the instabilities. Also, a lift of the plasma changes the

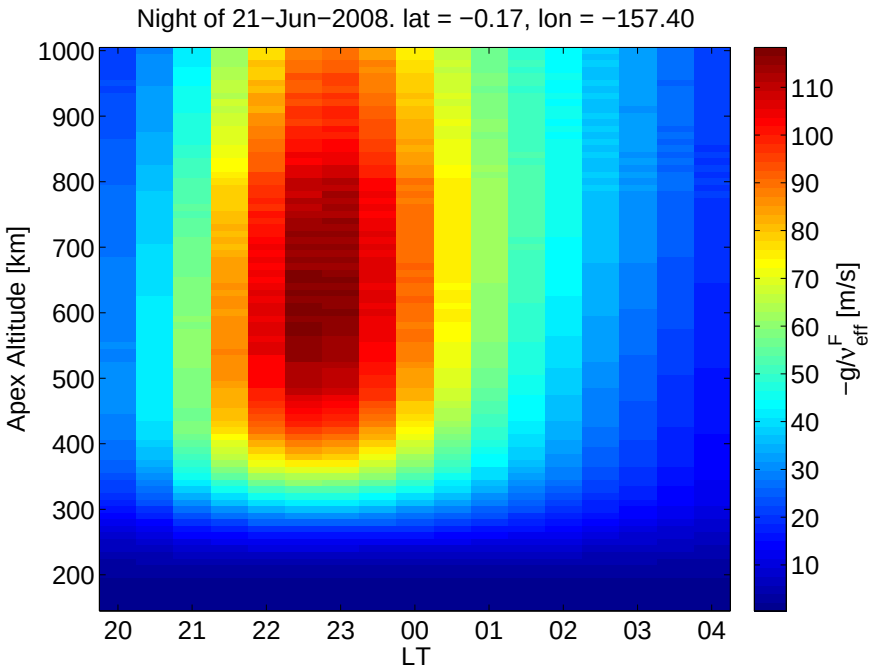

Figure 3.11: The second motion term, $-\vec{g}/\nu_{eff}^{F}$.

recombination rates, which impacts the plasma density and, again, affects the growth rate.

3.2.6 Assembly of γ_{RT}

Finally, to combine the previously obtained terms of Equation 3.1, γ_{RT} is assembled and plotted in Figure 3.13. For this example, positive growth rates are found just below the F peak— just under 300 km.

Notice that Figure 3.13 gives high positive growth rates after midnight. This is due to the large meridional winds from HWM (Figure 3.12) during those times. Such large wind gradients after midnight are believed to be an error in the model. To investigate, the altitude wind gradient was removed in U_m for hours after midnight, while all other terms were kept the same. Figure 3.14 shows the resultant growth rate. Here we see large positive growth rates before midnight and below the F layer.

Now that the basic model for γ_{RT} has been developed, we can simulate the RTI for many nights throughout the solar cycle and compare it with observed data. This is done in Chapter 4 with radar data obtained from Christmas Island. The model will prove to be a good indicator of certain seasonalites

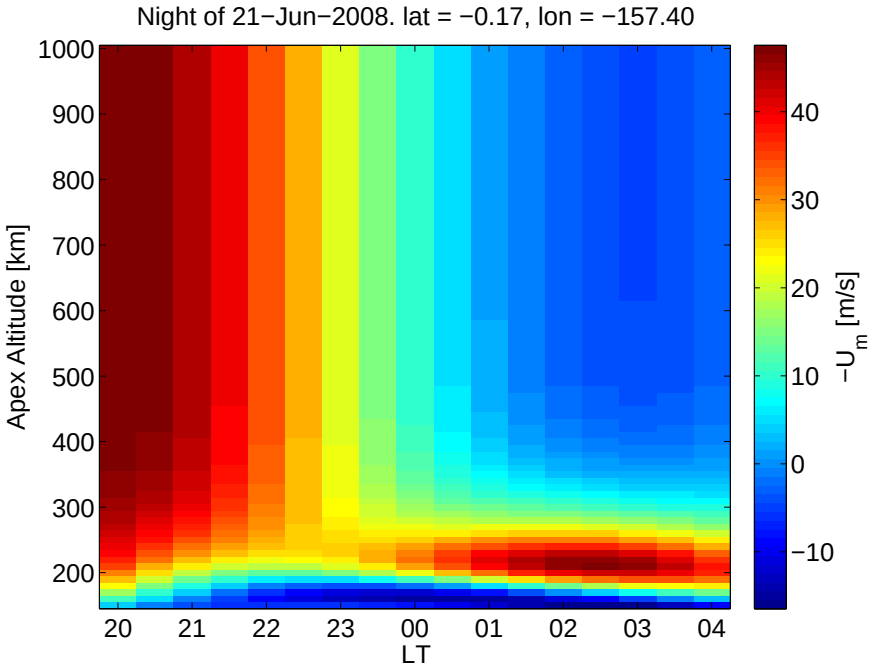

Figure 3.12: The negated meridonal component of the neutral wind along the magnetic field line profile using HWM 07.

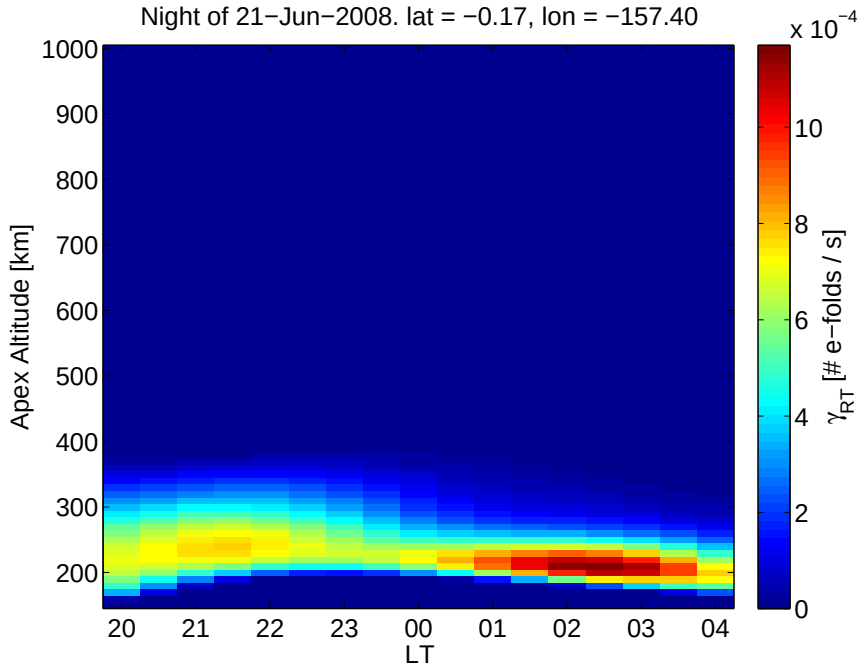

Figure 3.13: The Rayleigh–Taylor growth rate based on climatological models. Only positive growth rates are shown.

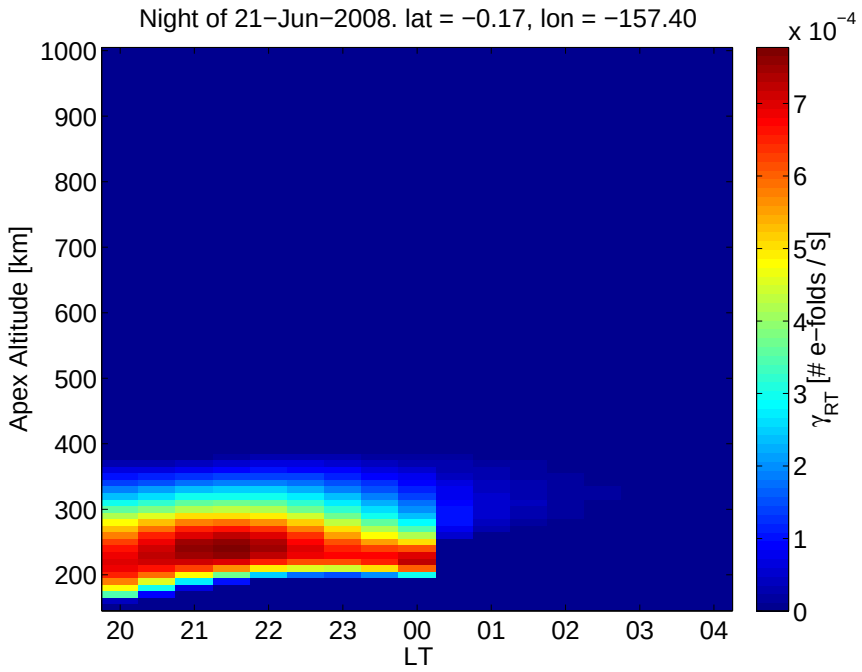

Figure 3.14: The Rayleigh–Taylor growth rate based on climatological models. Only positive growth rates are shown and the gradient term for post–midnight meridional winds has been removed.

of RTI. However, at times, the observations cannot be explained by the RTI alone and another mechanism must be referenced.

3.3 Perkins Instability

The Perkins instability applies momentum and continuity equations for both ions and electrons at mid–latitudes to explain how electron density, conductivity, and potential change in time and space [2]. In this section, we will give a brief overview of the Perkins instability including its equilibrium condition and growth rate.

The Perkins instability describes an instability mechanism at mid–latitudes that gives rise to nighttime medium–scale traveling ionospheric disturbances (MSTIDs). The growth rate of the Perkins instability describes to what extent MSTIDs are likely to occur and under what conditions they are likely to form. To arrive at the growth rate for the Perkins instability, we will start with the fundamental physical equations and then derive the equilibrium condition. Using these equations, the growth rate can then be determined.

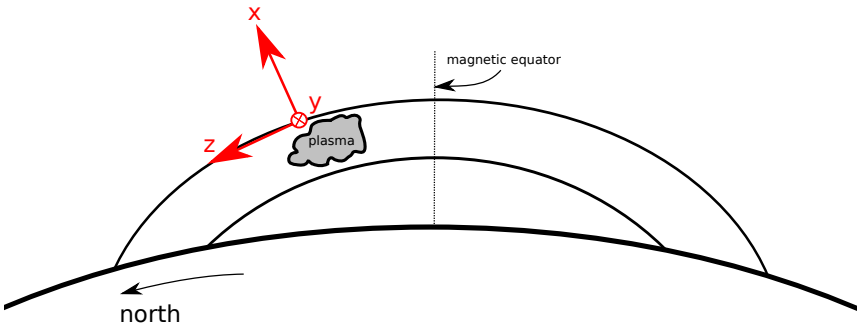

Figure 3.15: Coordinate system used when describing the Perkins instability.

To begin the development of these equations, a convenient coordinate system must first be defined.

3.3.1 Coordinate System

The coordinate system used to derive the Perkins instability aligns the z–axis with the magnetic field line. The coordinates are shown in Figure 3.15. The x–axis is referred to as "perpendicular–up," and the y–axis is in the eastern direction completing the right–hand rule. This particular coordinate system is advantageous because integrated quantities along the magnetic field lines can be introduced [2]. For example, the potential along the magnetic field line is constant and, hence, the value can be integrated along the field line. Doing so reduces the dimensional complexity of the equations. Also, by using integrated quantities, a given (x, y) coordinate pair defines a unique magnetic field line.

3.3.2 Fundamental Equations

In order to describe instabilities for mid–latitude regions, Perkins started with fundamental physics equations and developed an equilibrium condition, which was perturbed to study the growth rate for the instability. The derivation begins with the continuity and momentum equations for ions in a neutral gas:

$$\frac{\partial n_i}{\partial t} + \nabla \cdot (n_i \mathbf{v}_i) = 0 \tag{3.8}$$

Table 3.2: Terms in the momentum and continuity equations.

	Definition	Units
n_i	Ion density	number / m^3
$\mathbf{v}_i$	Ion velocity	m/s
$\mathbf{v}_e$	Electron velocity	m/s
p_i	Ion pressure	Pa
$\mathbf{E}$	Electric field	V/m
q	Fundamental charge	C
$\mathbf{B}$	Magnetic field strength	T
m_i	Ion mass	kg
$\mathbf{g}$	Acceleration due to gravity	m/s^2
ν_{in}	Ion–neutral collision frequency	collisions/s
ν_{ie}	Ion–electron collision frequency	collisions/s
$\mathbf{U}$	Neutral wind	m/s

$$n_i m_i D_t \mathbf{v}_i = -\nabla p_i + n_i q(\mathbf{E}+\mathbf{v}_i \times \mathbf{B}) + n_i m_i \mathbf{g} + n_i m_i \nu_{in}(\mathbf{U}-\mathbf{v}_i) + n_i m_i \nu_{ie}(\mathbf{v}_e - \mathbf{v}_i) \tag{3.9}$$

Terms used in these equations are defined in Table 3.2. Essentially, the change in the number of ions in time must be balanced by the spatial change of the ions (Equation 3.8), and momentum must be conserved in the system (Equation 3.9). Similar equations for the continuity and momentum for the electrons are given as

$$\frac{\partial n_e}{\partial t} + \nabla \cdot (n_e \mathbf{v}_e) = 0 \tag{3.10}$$

$$n_e m_e D_t \mathbf{v}_i = -\nabla p_e + n_e q(\mathbf{E}+\mathbf{v}_e \times \mathbf{B}) + n_e m_e \mathbf{g} + n_e m_e \nu_{en}(\mathbf{U}-\mathbf{v}_e) + n_e m_e \nu_{ei}(\mathbf{v}_i - \mathbf{v}_e) \tag{3.11}$$

These equations can be simplified based on the characteristics of the F region ionosphere [4]. The assumptions made are

1. The ions and electrons have a gyrofrequency because they are in a heavily magnetized fluid. This gyrofrequency has time scales much shorter than the motion of the ions and electrons, and therefore the gyrofre-

quency motion dominates. Therefore the left–hand sides of Equations 3.9 and 3.11 are set to 0.

2. The atmosphere is quasi–neutral, meaning that the number of ions and the number of electrons in the plasma are equal ($n_i \approx n_e$).

3. There are no "sources or sinks" in the macroscopic sense, which leads to the divergence–free condition, $\nabla \cdot \mathbf{J} = 0$. This enables us to combine Equations 3.8 and 3.10 as $\nabla \cdot (n_i \mathbf{v}_i) = \nabla \cdot (n_e \mathbf{v}_e)$.

4. Since an electron mass is much less than an ion mass, the ion–electron collision frequency (ν_{ie}) is negligible compared to the ion–neutral collision frequency (ν_{in}) in Equation 3.9.

5. The effect of gravity on the electrons is small, and thus the term in $n_e m_e \mathbf{g}$ can be ignored in Equation 3.11.

6. The atmosphere is isothermal, meaning that the pressure terms in Equations 3.9 and 3.11 can be written as $p = nk_BT$. Also, the temperatures of the electrons, ions, and neutrals are assumed to be the same.

With these assumptions, Equations 3.8 – 3.11 can be reduced to

$$\frac{\partial n}{\partial t} + \nabla \cdot (n \mathbf{v}_i) = 0 \tag{3.12}$$

$$0 = -k_B T \nabla n + nq(\mathbf{E} + \mathbf{v}_i \times \mathbf{B}) + nm_i \mathbf{g} + nm_i \nu_{in}(\mathbf{U} - \mathbf{v}_i) \tag{3.13}$$

$$0 = -k_B T \nabla n - nq(\mathbf{E} + \mathbf{v}_e \times \mathbf{B}) + nm_e \nu_{en}(\mathbf{U} - \mathbf{v}_e) + nm_e \nu_{ei}(\mathbf{v}_i - \mathbf{v}_e) \tag{3.14}$$

Next, $\mathbf{v}_i$ and $\mathbf{v}_e$ can be explicitly solved for in Equation 3.14, and from these velocities the perpendicular current, $\mathbf{J}_\perp = nq(\mathbf{v}_{i\perp} - \mathbf{v}_{e\perp})$, can be expressed. This $\mathbf{J}_\perp$ can be inserted into the divergence–free condition, $\nabla \cdot \mathbf{J}_\perp = 0$, and after some manipulation, substitution, and integration along the magnetic field line, Equations 3.12 – 3.14 can be written as [26]

Figure 3.16: The "Ping–Pong" model of the ionosphere at mid–latitudes. The ionosphere is supported by a southward neutral wind. After Kelley [3].

$$\frac{ge\cos D}{\Omega_i}\frac{\partial N}{\partial y}-\frac{2T}{e}\nabla_\perp^2\Sigma_P+\nabla_\perp\cdot[\Sigma_P\left(\mathbf{U}_\perp\times\mathbf{B}-\nabla_\perp\phi\right)]-\cos D\left(\frac{2T}{eH_n}+\frac{Mg}{e}\right)\frac{\partial\Sigma_P}{\partial x}=0 \tag{3.15}$$

$$\frac{\partial N}{\partial t}-(\nabla_\perp N)\cdot\left(\frac{1}{B}\nabla_\perp\phi\times\hat{z}\right)+\frac{g\cos D}{\Omega_i}\frac{\partial N}{\partial y}=0 \tag{3.16}$$

$$\frac{\partial\Sigma_P}{\partial t}+\nabla_\perp\Sigma_P\cdot\left(-\frac{1}{B}\nabla_\perp\phi\times\hat{z}+\frac{\mathbf{g}\times\hat{z}}{\Sigma_P}\right)-\Sigma_P\frac{\cos D}{BH_n}\frac{\partial\phi}{\partial y}-\frac{eg\sin^2 D}{\Omega BH_n}N-\Sigma_P\frac{U_z\sin D}{H_n}=0 \tag{3.17}$$

These equations describe how the integrated electron density (N), integrated Pedersen conductivity (Σ_P), and potential (ϕ) change in space and time. Using Equations 3.15 – 3.17, an equilibrium condition and growth rate can be derived. The equilibrium condition is found by setting the $\partial/\partial t$ terms to zero, and the growth rate is found by inserting a perturbation wave term, $\tilde{\Sigma}_P \propto e^{j(k_x x+k_y y-\omega t)}$, and looking at the exponential decay or growth of the resultant Σ_P [27].

3.3.3 Equilibrium Condition

In equilibrium, the ionosphere is supported by opposing forces. For the northern hemisphere, a southern neutral wind in combination with an eastward electric field can support plasma against the downward force of gravity. Figure 3.16 illustrates the southern neutral wind supporting the ionosphere. This "Ping–Pong" model shows that the hairdryer (neutral wind) pushes air against the ramp (magnetic fields) to hold the Ping–Pong ball (plasma) in place [28].

The equilibrium condition for the Perkins equations is given as [15]

$$\frac{(\mathbf{U} \times \mathbf{B} + \mathbf{E})_{\text{eastern}} \cos D}{|\mathbf{B}|} = \frac{g}{< \nu_{in} >} \sin^2 D \tag{3.18}$$

where $\mathbf{U}$ is the neutral wind, $\mathbf{E}$ is the background electric field, D is the dip angle, and g is the acceleration due to gravity. The integrated ion–neutral collision frequency in the F region, $< \nu_{in} >$, is expressed as [23]

$$< \nu_{in} > = \frac{\int_b^t n \nu_{in} \, dz}{\int_b^t n \, dz} \tag{3.19}$$

where n is the electron density, ν_{in} is the ion–neutral collision frequency, and dz represents integration along the magnetic field line. The integration limits b and t represent the *bottomside* and *topside* of the F layer, respectively. Equation 3.19 is a weighted average of ν_{in}. This term is the same as Equation 3.5 but has been notationally changed to keep consistent with Perkins original equations.

In Equation 3.18, the only free parameter is $< \nu_{in} >$. For a given location, the dip angle and magnetic field strength stay constant for timescales of less than a day. Therefore, if there is a change in either the background electric field or neutral wind, the plasma will seek out a new height to maintain equilibrium corresponding to the new value of $< \nu_{in} >$.

By taking the eastern component of the cross–product, Equation 3.18 can be reduced to

$$U_s \sin D \cos D + \frac{E_{\text{eastern}} \cos D}{|\mathbf{B}|} = \frac{g}{< \nu_{in} >} \sin^2 D \tag{3.20}$$

where U_s is the southern neutral wind.

An example of a $< \nu_{in} >$ profile is shown in Figure 3.17. The term $< \nu_{in} >$ decreases exponentially with increasing altitude. For the northern hemisphere, if the eastern background electric field is increased, the left–hand side of Equation 3.20 will increase. To maintain equilibrium, $< \nu_{in} >$ must decrease, which corresponds to the plasma seeking a higher altitude layer. Intuitively this makes sense: an eastward electric field supports the plasma layer. Likewise, an increase in the southern wind will increase the left–hand side of the equation, resulting in a height increase as well. This agrees with the "Ping–Pong" model of Figure 3.16.

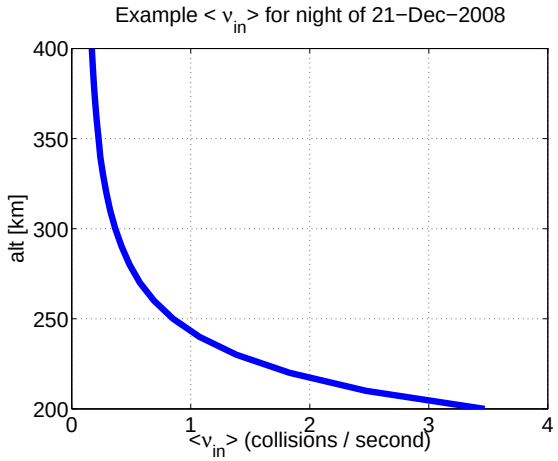

Figure 3.17: A typical $< \nu_{in} >$ profile.

Table 3.3: Terms of the Perkins instability growth rate.

	Definition	Units
D	Dip angle of the magnetic field	degrees
$\vec{B}$	Magnetic field	T
H_n	Scale height of the neutral density	m
$\vec{E}_0$	Background electric field	V/m
$\vec{k}$	Perturbation wave vector	1/m
$\vec{U}_{0\perp}$	Neutral wind in the x and y direction	m/s
U_{0z}	Neutral wind along the magnetic field line	m/s

3.4 Perkins Instability Growth Rate

The Perkins instability growth rate describes the rate at which conductivity bands decay or grow. Zhou and Mathews did an analysis of the growth rate including the neutral wind term [27]. The growth rate is the resultant perturbed conductivity wave's imaginary part:

$$\gamma_P = \frac{\cos D}{BH_n}\left[-E_{0y} + \frac{k_y}{k^2}\vec{k}\cdot\left(\vec{E}_0 + \vec{U}_{0\perp}\times\vec{B}\right)\right] + \frac{\sin D}{H_n}U_{0z} \tag{3.21}$$

Table 3.3 describes the parameters of Equation 3.21 and their corresponding units. Figure 3.18 shows two plasma slabs that have been offset in vertical

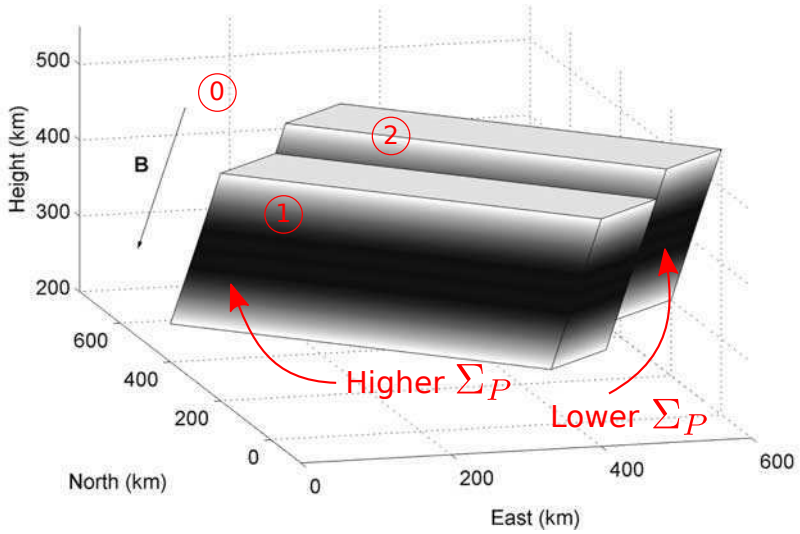

Figure 3.18: Slabs of raised and lowered plasma. After Zhou and Mathews [27].

space due to an initial wave vector. The lowered slab has a higher integrated Pedersen conductivity (Σ_P) than its surroundings (which, pictorially, is not shown) because $\Sigma_P \propto \ < \nu_{in} > \ \propto \text{alt}^{-1}$. Similarly, the raised band of Σ_P will have lower integrated Pedersen conductivity.

A top–view of Figure 3.18 is shown in Figure 3.19. Using the divergence–free condition, $\nabla \cdot \mathbf{J} = 0$ (no free charges in the macroscopic sense), the current normal to the interfaces must be the same: $J_{0n} = J_{1n} = J_{2n}$. The boundary conditions require the tangential electric fields across the two interfaces must be the same, $\hat{n} \times (\mathbf{E}_2 - \mathbf{E}_1) = 0$. Since $E_{0t} = E_{1t} = E_{2t}$ and $\Sigma_1 > \Sigma_0 > \Sigma_2$, then $J_{1t} > J_{0t} > J_{2t}$.

Now that J_{1t} is increased, the eastward current is reduced in region 1 of Figure 3.19 because there is a westward component to J_{1t}. If the eastward electric field is reduced, the plasma layer will drop. This creates a positive feedback loop: the layer drops, J_{1t} is increased, and the eastward electric field is reduced. In this way, the system goes unstable. Equation 3.21 describes the rate at which this process happens and is a function of the initial vector wave perturbation.

Using the climatological models, an example plot of the Perkins growth rate (Equation 3.21) is simulated in Figure 3.20. The white space region is where the model is not valid (further explained in Chapter 4), and thus the value of γ_P was discarded for that particular point. This model was

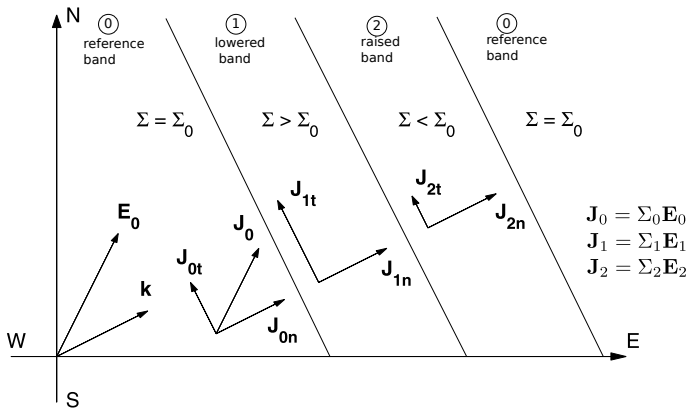

Figure 3.19: Top view of the alternating bands of plasma. After Zhou and Mathews [27].

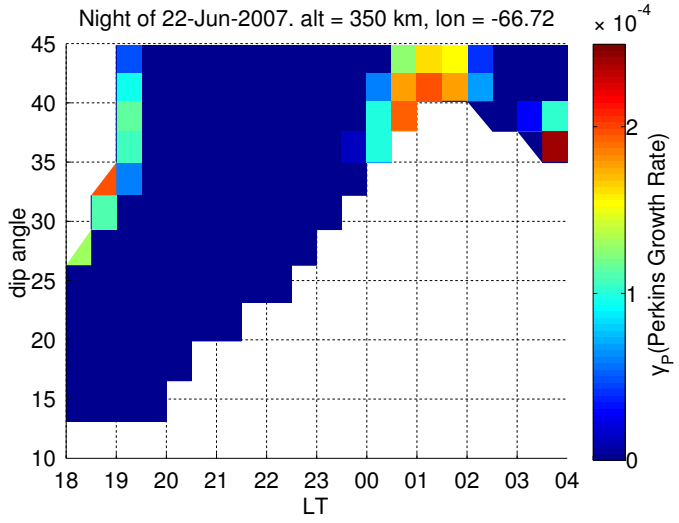

Figure 3.20: Example simulation of the Perkins instability for a variety of dip angles and local times.

simulated for a variety of dip angles (corresponding to magnetic latitude). Most notable are the positive growth rate values for post–midnight at mid–latitude locations (at a dip angle of around 45°). As shown in Chapter 4, this positive growth rate will explain ESF events not accounted for by the RTI.

The electric field model used was obtained from a combination of the drift data from Arecibo [29], an observatory located in Puerto Rico (a mid–latitude location), and the Scherliess and Fejer (S–F) model (based on data from equatorial locations). Knowing the drifts and the magnetic field strength, the electric field can be found via Equation 3.7. A simple linear interpola-

tion between the magnetic equator (S–F) and Arecibo's latitude is used to estimate the electric field at all latitudes.

3.5 Conclusion

In this chapter, two instability mechanisms were introduced: the RTI to explain ionospheric disturbances at low latitudes and the Perkins instability at mid–latitudes. Climatological models were used to calculate the different components of the RTI growth rate, and it was shown how each portion affects the growth rate. A description of the derivation of the Perkins instability was given. This lead to the equilibrium condition and growth rate for this instability mechanism. In the next chapter, the RTI and Perkins growth rates will be used to describe radar data of ESF collected at an equatorial site in the Pacific.

CHAPTER 4

SIMULATIONS

In this chapter, simulations of the two instability mechanisms are carried out: the Rayleigh–Taylor instability growth rate (Equation 3.1) at equatorial regions and the Perkins instability growth rate (Equation 3.21) at mid–latitudes. The simulations are similar to Figures 3.13 and 3.20, but have been extended to include several years in order to show seasonality characteristics. These simulations will be compared with radar data collected at Christmas Island, an observatory in the Pacific. It will be shown that the RTI cannot fully explain all ESF events, which gives motivation for simulating the Perkins instability at mid–latitudes. The MSTIDs developed by the Perkins instability are hypothesized to impact equatorial events [1]. The simulations of MSTIDs at mid–latitudes will further support the observational evidence of mid–latitude coupling into equatorial regions.

4.1 Christmas Island Radar Data

In order to study the occurrence of irregularities in the low–latitude ionosphere, a 50–MHz radar was installed on Christmas Island Radar (CXI) facility ($2.0°N$, $-157.4°E$) in Kiribati by the Air Force Research Laboratory [13]. A map of the location of CXI is shown in Figure 4.1. The antenna is a 100 $\times$ 100 m co–co–type array with two stationary beams in the east and north directions. The east beam has an elevation angle of 60.5° and azimuth of 90.0°, while the north beam has an elevation angle of 84.5° with an azimuth of 0.0°. The backscatter of the radar return is measured at CXI allowing the observation of the altitude and temporal distribution in 3–m irregularities. Currently, every 75 s the radar provides signal–to–noise ratio (SNR) information in altitude bins of 10 km.

The data are sorted into 15–minute bins and classified as either having

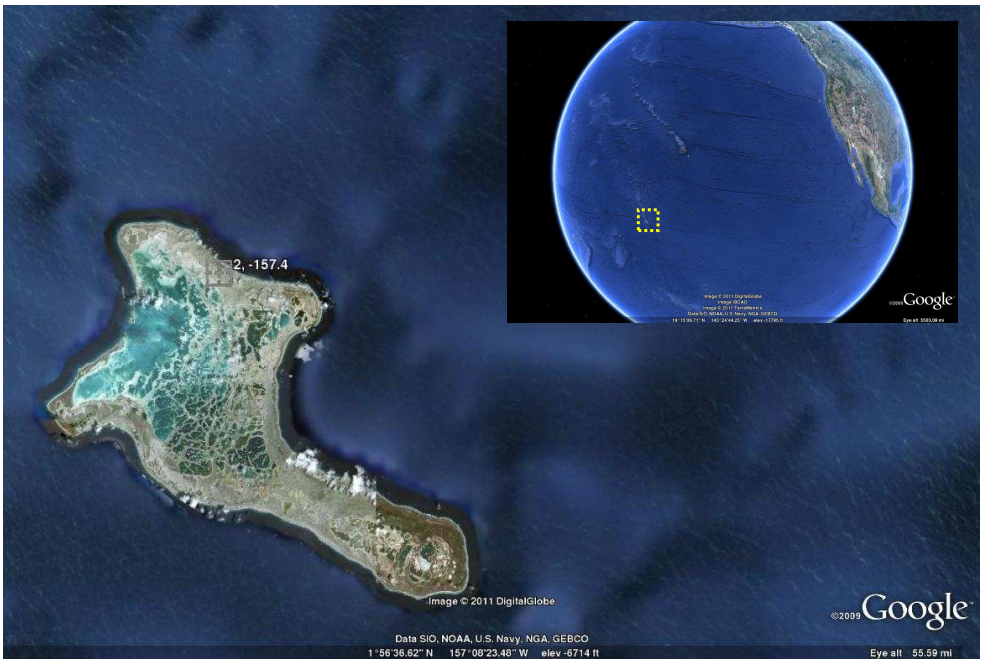

Figure 4.1: Christmas Island (CXI) radar facility in Kiribati.

or not having a SNR > -10 dB for altitudes above 200 km. The radar returns having an SNR greater than -10 dB are indicative of an irregularity. Then, a 20–day sliding window was applied to this binary value and the averaged results were tallied. This was done for each day from roughly 2002 through 2009 (although data were unavailable for some periods of time due to instrument maintenance). The results are shown in Figure 4.2 (top). These data have the signature of disturbances in the ionosphere which are indicative of Equatorial Spread F (ESF). In other words, Figure 4.2 (top) represents an indicator of ESF throughout the night for several years as measured at Christmas Island.

4.2 Rayleigh–Taylor Instability Simulation

Using the RTI growth model developed in Section 3.2 for the CXI location, the growth rate can be compared to the radar backscatter data. The RTI growth rate was calculated throughout the night for a given day in altitude ranges of 200–400 km. Then, the maximum RTI growth rate was selected across all altitudes and this "strip" for that day was placed into the yearly trend in the bottom of Figure 4.2. This process was repeated every day from

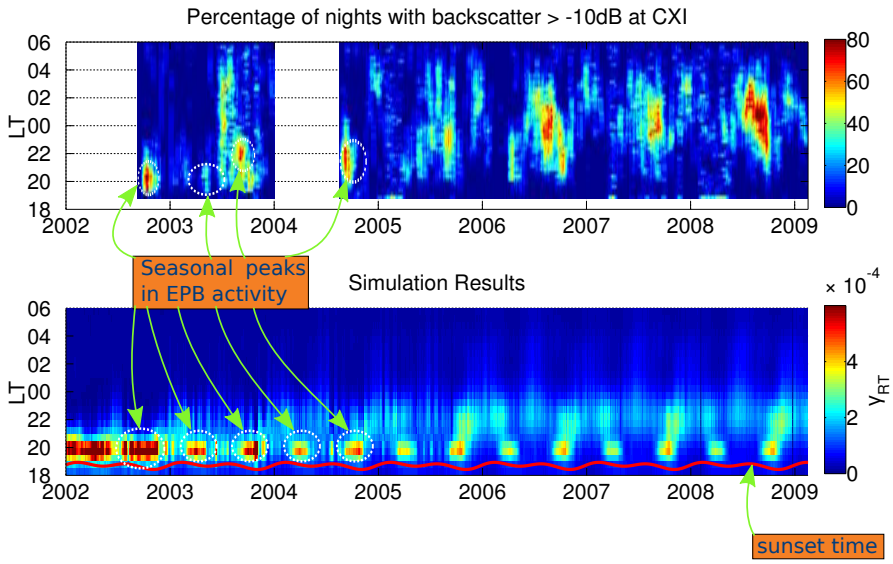

Figure 4.2: (top) Statistical information of radar backscatter at the Christmas Island radar throughout a solar cycle. The red areas indicate ESF. After Miller et al. [13]. (bottom) The RTI growth rate γ_{RT} for the same location and time in order to make a comparison with the indicators of ESF above.

2002 through 2009 and gives the maximum modeled growth rate for a given time of the night at a specific day.

There are interesting similarities between the radar data and modeled growth rate in Figure 4.2. Early in the solar cycle, the radar backscatter correlates with the modeled RTI growth rate quite well: plasma depletions from the radar data (top) are reflected as high growth rates in the modeled (bottom). The majority of ESF events in the CXI data (and likewise, the high growth rates from the model) occur just after sunset, noted by the red line in the bottom of Figure 4.2. Since the RTI growth rate is indicative of ESF events in the probabilistic sense, the modeled γ_{RT} is in good agreement with the seasonalities of the post–sunset ESF events given by the CXI radar data for post–sunset activity.

However, from Figure 4.2 it appears that not all ESF observed at CXI can be explained by the RTI. Interestingly, there is post–midnight activity during 2005–2009 (years of declining solar activity) at CXI that the RTI does not predict. It has been hypothesized that these cases of ESF are the result of a seed mechanism from the electric fields of MSTIDs [1], specifically the polarization electric field of a MSTID. Under this hypothesis, the polarization

electric field internal to the MSTID maps along the magnetic field lines to equatorial regions. This electric field can couple into the F region and initiate the RTI [30]. Observational evidence of this coupling has been presented by Miller et al. [1] using a combination of all–sky imagers and radar backscatter in a field–aligned geometry.

To further investigate this claim, the RTI growth rate (Equation 3.1) is perturbed with an additional motion term, indicative of a polarization electric field driven by an MSTID. There have been studies of MSTID drift velocities, and it has been found that the electric fields can cause drifts up to 50 m/s [31]. Velocities of 25 m/s and 50 m/s are added to the numerical model as an extra perturbation vertical motion term in the growth rate equation to study their effects on the RTI.

The observational evidence suggest that the seeding of ESF by MSTIDs is a solar minimum phenomenon [1]. To investigate this claim, the first row of Figure 4.3 simulates a solar maximum day, while the second row simulates a solar minimum day. The corresponding $f_{10.7}$ values are 196.5 and 79.1, respectively. Each column represents a different amount of perturbation motion term: 0 m/s, 25 m/s, and 50 m/s, respectively. For the solar minimum night, the extra motion term increases the growth rate to an appreciable amount. Most notably, this increase of the growth rate occurs around local midnight, which is what the observations (top of Figure 4.2) reflect. Therefore, if an extra motion term were to occur (a seed mechanism), it would help to explain the post–midnight solar minimum activity of the CXI radar. It is proposed that this extra perturbation term is from MSTIDs, which are often attributed to the Perkins instability. To further investigate this claim, a study of the Perkins instability will be conducted next.

4.3 Perkins Instability Simulation

The Perkins growth rate (Equation 3.21) is dependent on the direction of the incident wave vector $\mathbf{k}$. In fact, $\gamma_P \propto \sin\theta \sin(\theta - \alpha)$, where θ is the angle between the background electric field and magnetic east and α is the angle between $\mathbf{k}$ and magnetic east. To validate the model, a simulation of γ_P was carried out for a variety of $\mathbf{k}$ corresponding to wavelengths ranging from 50 to 500 km, and for all angles of α. Figure 4.4 shows the result. The growth

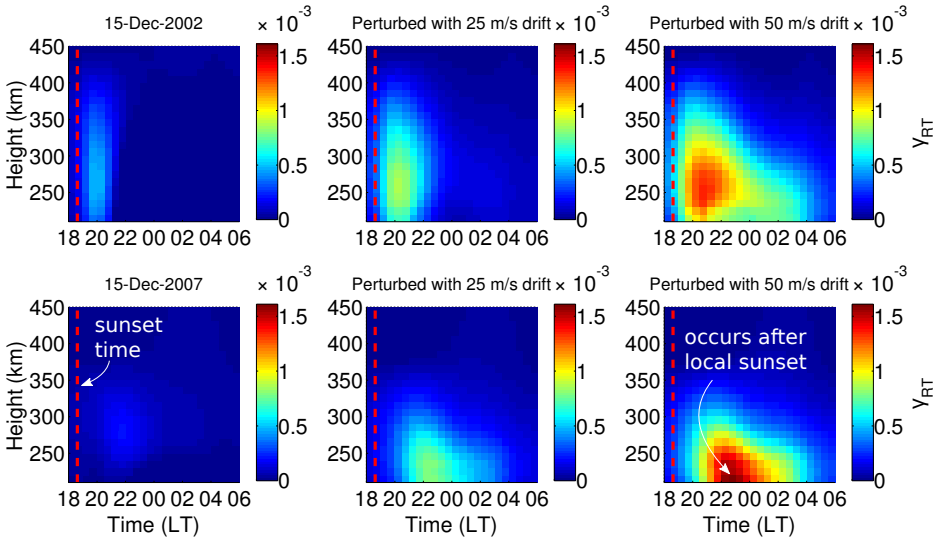

Figure 4.3: The perturbed model of the RTI.

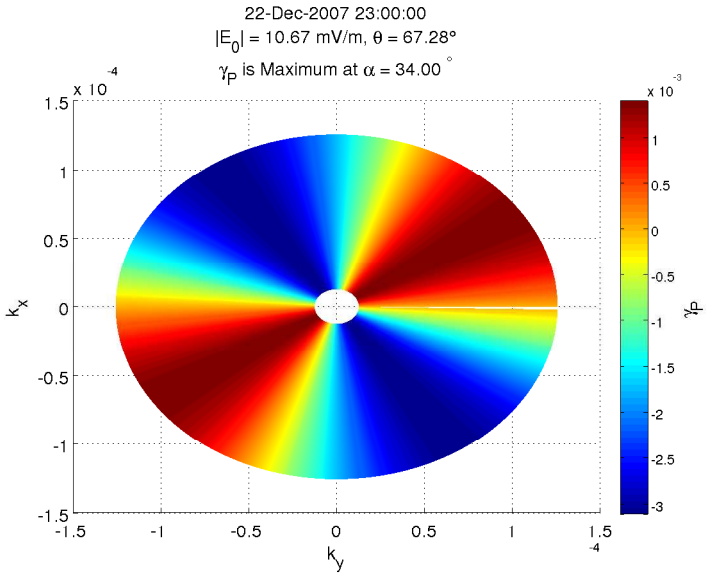

Figure 4.4: γ_P as a function of angle and magnitude. γ_P maximizes for half the angle of the electric field.

rate maximizes for $\alpha = \theta/2$, which agrees with Perkins theory [15]. Also, the theory predicts the growth rate as being independent of the perturbation wavelength. Figure 4.4 reflects this as γ_P does not vary significantly in the radial direction.

When running the growth rate simulation, it is important to understand that γ_P is only valid under certain conditions. Specifically, the equilibrium condition (Equation 3.18) must provide a reasonable $< \nu_{in} >$ associated with a particular altitude that is in the F region. For example, in equatorial regions where the dip angle is small, the plasma cannot travel much vertical distance along the magnetic field lines, meaning that the Perkins stability constraint cannot be met. Also, if there is a strong westward electric field, the left–hand side of Equation 3.18 will be negative, meaning that the required $< \nu_{in} >$ is negative, resulting in an unrealistic scenario. To resolve this issue, the values of γ_p that have a required $< \nu_{in} >$ that provide an unrealistic equilibrium altitude are discarded. In other words, the calculated growth rate of Equation 3.21 is only valid for $0 \leq < \nu_{in} > \leq 4$, which corresponds to an equilibrium altitude of roughly 200 – 400 km (see Figure 3.17).

To build the summary image analogous to Figure 4.2 (bottom), the following procedure was carried out. A nightly run of the Perkins growth rate was computed, shown in Figure 4.5. Then, a particular dip angle was chosen. In this case a location having the same longitude of CXI with a dip angle of 45° was selected. This "strip" is placed into the yearly summary for that particular day, and this was repeated for dates corresponding with Figure 4.2. Since electric fields can map to the equator from either the northern or southern hemisphere, the simulation was run at a dip angle of $-45°$ as well, and the maximum growth rate between the two was selected for the summary plot.

The results of the modeled γ_P for the northern and southern hemispheres are shown in Figure 4.6. For each case, the model is only valid during certain seasons of the year. Production of plasma is higher for days that have longer daylight hours, which is a function of day of year and location. The collision frequency is proportional to the amount of plasma present, and as shown in Equation 3.18, the equilibrium condition depends on ν_{in}. Notice that for the northern region the model is valid for days near the June solstice, while for the southern region it is valid for days near the December solstice. The pre–midnight high growth rates are primarily from the southern location

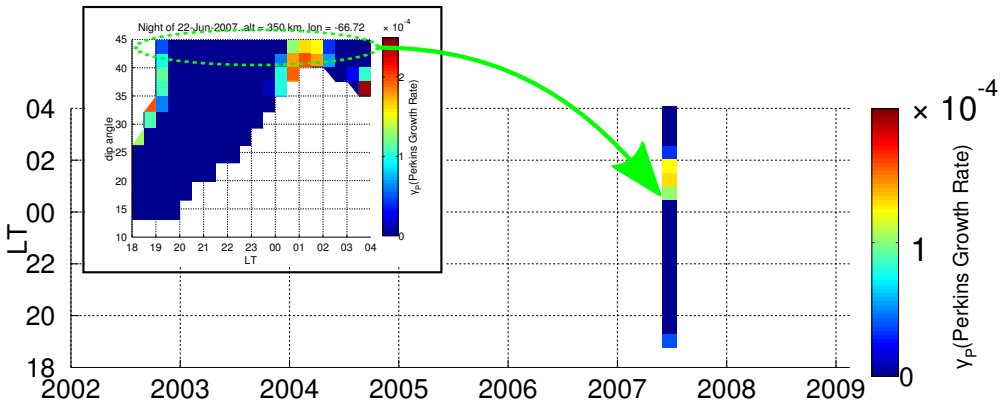

Figure 4.5: Using the γ_P model to build a summary image.

(December solstice days), but as will be shown, this is the same time period in which the the radar data recorded post–midnight activity.

The comparison results of the radar data and the model are shown in Figure 4.7. The bottom portion of this figure is the maximum value between the two plots in Figure 4.6. In general, the model is in good agreement with the radar backscatter data. For solar minimum nights, there are positive growth rates for the Perkins instability at dip angles of $\pm 45°$. During nights near the December solstice, the mid–latitude, CXI longitude location has positive growth rates for times before midnight. Structures developed during this time take a few hours to travel toward the equatorial region to be observed at CXI. There is about a 6–hour time delay between the large modeled γ_P and post–midnight activity from the radar data. Given that the distance between $\pm 45°$ magnetic latitude and CXI is about 2700 km, this corresponds to an MSTID traveling at 125 m/s, which is toward the upper limit of observational velocities [14]. Because of the high conductivity along the magnetic field lines, it is plausible that the electric fields internal to MSTIDs map toward the equator and could possibly initiate ESF there.

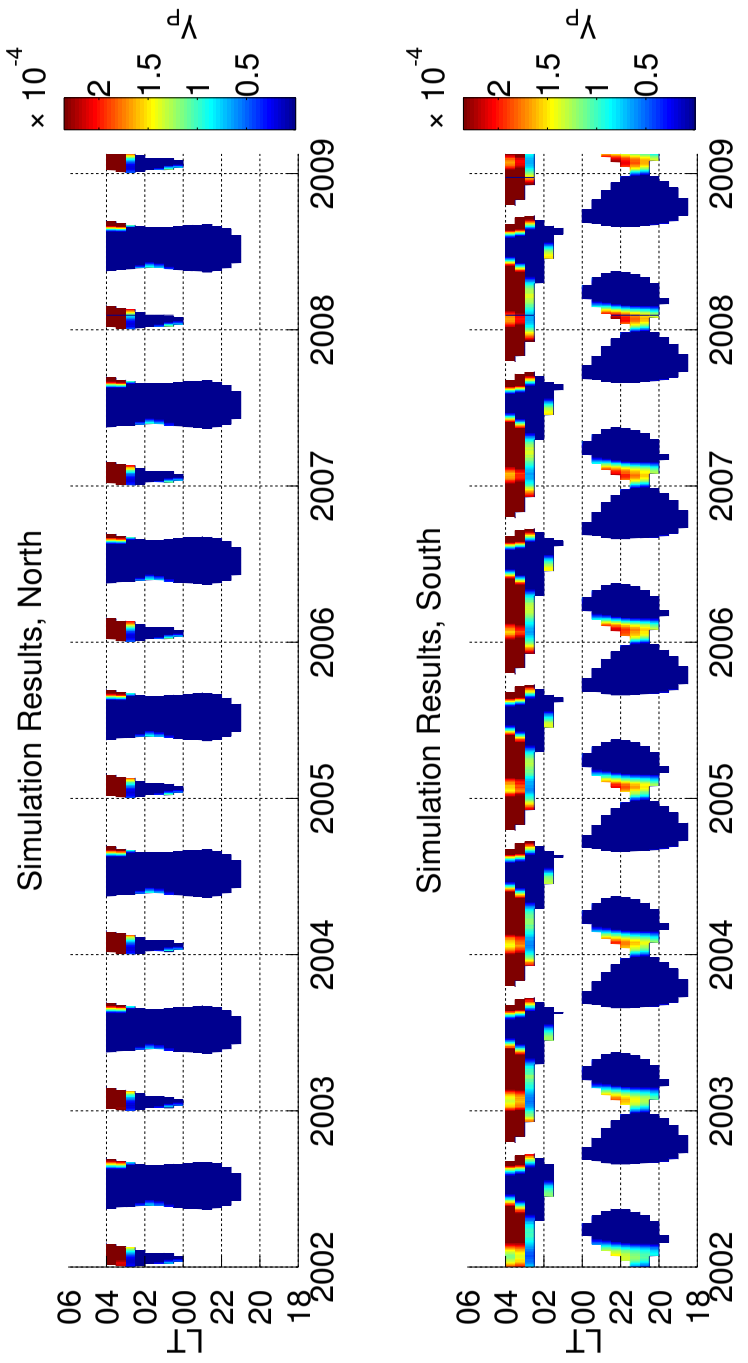

Figure 4.6: The Perkins instability growth rate (γ_P) for $+45°$ (top) and $-45°$ (bottom) magnetic latitude.

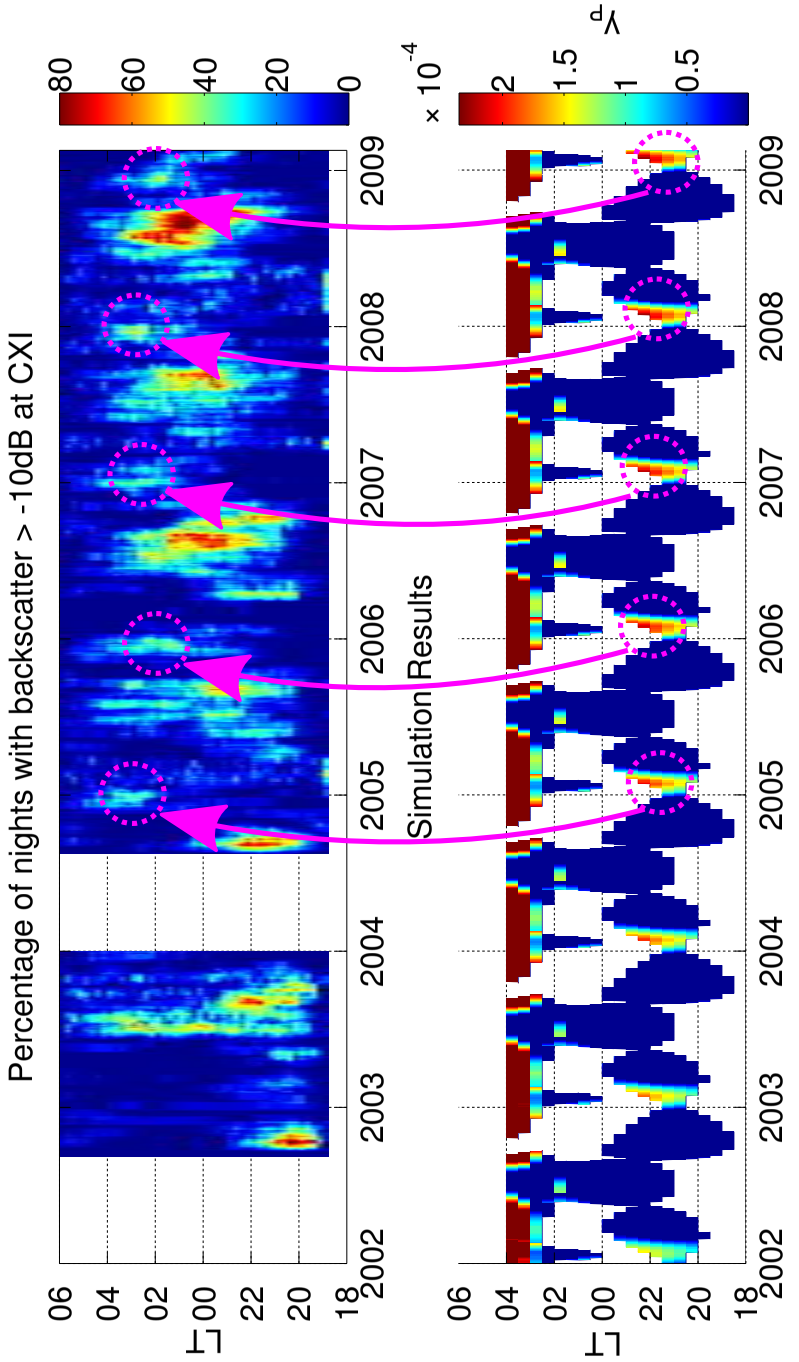

Figure 4.7: Comparison of the modeled γ_P (bottom) with the CXI radar data (top). The bottom plot is the maximum value between the two plots of Figure 4.6.

CHAPTER 5

CONCLUSION

5.1 Conclusions

This thesis provided the climatological modeling support to the observational evidence of MSTIDs seeding ESF. The models were based on equations for the growth rates of the Rayleigh–Taylor instability and Perkins instability. These two equations describe how fast ionospheric instabilities develop at both low and mid–latitudes, respectively. The simulations of the RTI and Perkins growth rate were compared with radar data from Christmas Island, a remote observatory in the Pacific. The post–sunset seasonalities of the RTI corresponded well with the radar data, but post–midnight activity at CXI was not completley explained by the RTI growth rate model. However, the Perkins instability growth rate model did explain the post–midnight activity, further advocating for the existence of coupling between low and mid–latitudes.

Chapter 2 provided an introduction to the basic composition of ionosphere. It discussed how the region is anisotropic, meaning that the conductivity in the ionosphere is represented as a tensor term. The irregularities were introduced for both low– and mid–latitude regions, with example time sequence plots of instabilities as well as statistical occurrence rates for each case. Finally, various climatological models were given which served as a basis for the parameters embedded in the developed growth rate models.

The instability mechanisms were explored in Chapter 3. The theory behind the Rayleigh–Taylor instability was given and the growth rate equation was provided. This equation was broken down into individual terms, and each was plotted for an example night in order to view the contributions from each term. The Perkins instability was introduced afterward as an instability mechanism for mid–latitude locations. An example plot of the Perkins growth

rate was provided for a solar minimum night.

Chapter 4 provided simulations pertinent to observed data. First, radar data were shown from the Christmas Island observatory in Kiribati, and it was explained how this instrument provides information about ESF. Then, the Rayleigh–Taylor growth rate was simulated at this location. It was shown that the corresponding ESF seasonalities corresponded well with the RTI simulation. However, there were irregularities during post–midnight, solar minimum days that the RTI did not explain. To resolve this issue, the Perkins instability growth rate was simulated for a location having the same longitude of CXI but at a mid–latitude. It was found that the Perkins instability provided the high growth rates indicative of MSTIDs. Thus, it was found to be very plausible that developed MSTIDs could couple into low latitudes and initiate ESF there.

5.2 Future Work

In order to further provide simulation evidence of MSTID seeding, more modeling work must be completed. An outstanding study that remains is to simulate the ionosphere at mid–latitudes from a purely physics–based model that self–consistently solves for the potential. The development of the polarized electric fields from this simulation would provide additional support to the growth rate simulations conducted in this thesis. For example, Figure 4.3 utilized drift velocities from observations. These drift velocity measurements would be replaced by the results of the physics–based model. In this way, the simulations would provide a more complete picture of the modeling of ESF development.

The physics–based model would also provide the electric field term used for the Perkins instability growth rate. In this thesis, the electric field was obtained from a simple linear interpolating function constructed from measurements at low and mid–latitudes. Having a global model of the electric field would provide a more realistic scenario of the Perkins instability growth rate.

REFERENCES

[1] E. Miller, J. Makela, and M. Kelley, "Seeding of equatorial plasma depletions by polarization electric fields from middle latitudes: Experimental evidence," *Geophysical Research Letters*, vol. 36, no. 18, pp. 1–5, Sep. 2009.

[2] F. Perkins, "Spread F and ionospheric currents," *Journal of Geophysical Research*, vol. 78, no. 1, pp. 218–226, 1973.

[3] M. C. Kelley, *The Earth's Ionosphere*. Burlington, MA: Academic Press, 2009.

[4] C. A. Miller, "On gravity waves and the electrodynamics of the mid–latitude ionosphere," Ph.D. dissertation, Cornell University, Ithaca, NY, 1996.

[5] D. Farley, "A theory of electrostatic fields in a horizontally stratified ionosphere subject to a vertical magnetic field," *Journal of Geophysical Research*, vol. 64, no. 9, pp. 1225–1233, 1959.

[6] L. Berkner and H. W. Wells, "F–region ionosphere investigation at low altitudes," *Terrestrial Magnetism and Atmospheric Electricity*, vol. 39, no. 3, pp. 215–230, 1934.

[7] M. C. Kelley, M. F. Larsen, C. Lahoz, and J. P. McClure, "Gravity-Wave Initiation of Equatorial Spread F— A Case Study," *Journal of Geophysical Research–Space Physics*, vol. 86, no. NA11, pp. 9087–9100, 1981.

[8] J. J. Makela, "A review of imaging low-latitude ionospheric irregularity processes," *Journal of Atmospheric and Solar-Terrestrial Physics*, vol. 68, no. 13, pp. 1441–1458, 2006.

[9] M. Mendillo, J. Baumgardner, D. Nottingham, and J. Aarons, "Investigations on the thermospheric-ionospheric dynamics with 6300-Å images from the Arecibo Observatory," *Journal of Geophysical Research*, vol. 102, no. A4, pp. 7331–7343, 1997.

[10] A. Saito, S. Fukao, and S. Miyazaki, "High resolution mapping of TEC perturbations with the GSI GPS network over Japan," *Geophysical research letters*, vol. 25, no. 16, pp. 3079–3082, 1998.

[11] J. Röttger, "Wave-like structures of large-scale equatorial spread-F irregularities," *Journal of Atmospheric and Terrestrial Physics*, vol. 35, no. 6, pp. 1195–1196, 1973.

[12] L. Gentile, W. Burke, and F. Rich, "A climatology of equatorial plasma bubbles from DMSP 19892004," *Radio Science*, vol. 41, no. 5, p. RS5S21, 2006.

[13] E. Miller, J. Makela, K. Groves, M. Kelley, and R. Tsunoda, "Coordinated study of coherent radar backscatter and optical airglow depletions in the central Pacific," *Journal of Geophysical Research*, vol. 115, no. A6, pp. 1–12, June 2010.

[14] K. Shiokawa, C. Ihara, Y. Otsuka, and T. Ogawa, "Statistical study of nighttime medium-scale traveling ionospheric disturbances using midlatitude airglow images," *Journal of Geophysical Research*, vol. 108, no. A1, p. 1052, 2003.

[15] F. Garcia, M. Kelley, J. Makela, and C.-S. Huang, "Airglow observations of mesoscale low-velocity traveling ionospheric disturbances at midlatitudes," *Journal of Geophysical Research*, vol. 105, no. A8, p. 18407, 2000.

[16] J. M. Picone, "NRLMSISE-00 empirical model of the atmosphere: Statistical comparisons and scientific issues," *Journal of Geophysical Research*, vol. 107, no. A12, pp. 1–16, 2002.

[17] D. Bilitza and B. Reinisch, "International Reference Ionosphere 2007: Improvements and new parameters," *Advances in Space Research*, vol. 42, no. 4, pp. 599–609, Aug. 2008.

[18] A. Hedin et al., "Revised global model of thermosphere winds using satellite and ground-based observations," *Journal of Geophysical Research*, vol. 96, no. A5, pp. 7657–7688, 1991.

[19] L. Scherliess and B. Fejer, "Radar and satellite global equatorial F region vertical drift model," *Journal of Geophysical Research*, vol. 104, no. A4, pp. 6829–6842, 1999.

[20] S. Maus et al., "The 10th generation international geomagnetic reference field," *Physics of the Earth and Planetary Interiors*, vol. 151, no. 3-4, pp. 320–322, Aug. 2005.

[21] J. W. Dungey, "Convective diffusion in the equatorial F region," *Journal of Atmospheric and Terrestrial Physics*, vol. 9, no. 5-6, pp. 304–310, 1956.

[22] C. Martinis, M. Mendillo, and J. Aarons, "Toward a synthesis of equatorial spread F onset and suppression during geomagnetic storms," *Journal of Geophysical Research*, vol. 110, no. A7, pp. 7306–7319, 2005.

[23] R. Tsunoda, "On the coupling of layer instabilities in the nighttime midlatitude ionosphere," *Journal of Geophysical Research*, vol. 111, no. A11, pp. 1–14, Nov. 2006.

[24] R. Tsunoda, "Control of the seasonal and longitudinal occurrence of equatorial scintillations by the longitudinal gradient in integrated E region Pedersen conductivity," *Journal of Geophysical Research*, vol. 90, no. A1, pp. 447–456, 1985.

[25] P. Sultan, "Linear theory and modeling of the Rayleigh-Taylor instability leading to the occurrence of equatorial spread F," *Journal of Geophysical Research*, vol. 101, no. A12, pp. 26 875–26 891, 1996.

[26] Q. N. Zhou, "A numerical investigation of the Perkins instability equations by the pseudo–spectral method," Ph.D. dissertation, Pennsylvania State University, State College, PA, 2004.

[27] Q. Zhou and J. D. Mathews, "On the physical explanation of the Perkins instability," *Journal of Geophysical Research*, vol. 111, pp. 1–7, 2006.

[28] M. Kelley, J. Makela, and M. Vlasov, "Further studies of the Perkins stability during Space Weather Month," *Journal of Atmospheric and Solar-Terrestrial Physics*, vol. 65, no. 10, pp. 1071–1075, July 2003.

[29] B. G. Fejer, "F region plasma drifts over Arecibo: Solar cycle, seasonal, and magnetic activity effects," *Journal of Geophysical Research*, vol. 98, no. A8, pp. 13 645–13 652, 1993.

[30] R. Tsunoda, "Seeding of equatorial plasma bubbles with electric fields from an Es-layer instability," *Journal of Geophysical Research*, vol. 112, no. A6, pp. 1–13, June 2007.

[31] M. Kelley, J. Makela, A. Saito, N. Aponte, M. Sulzer, and S. González, "On the electrical structure of airglow depletion/height layer bands over Arecibo," *Journal of Geophysical Research*, vol. 27, no. 18, pp. 2837–2840, 2000.

AUTHOR'S BIOGRAPHY

Timothy Matthew Duly graduated summa cum laude from The Ohio State University in 2009 with a Bachelor of Science in Electrical Engineering. After graduating he pursued graduate school in the Remote Sensing and Space Sciences group in the Department of Electrical and Computer Engineering at the University of Illinois at Urbana–Champaign. He plans to pursue a P.h.D. after earning his master's degree.